

1 **Decomposition of the horizontal wind divergence**
2 **associated with the Rossby, inertia-gravity, mixed**
3 **Rossby-gravity and Kelvin waves on the sphere**

4 **Valentino Neduhal¹, Nedjeljka Žagar¹, Frank Lunkeit¹, Inna Polichtchouk²,**
5 **Žiga Zapltnik³**

6 ¹Meteorological Institute, Center for Earth System Research and Sustainability, Universität Hamburg,
7 Germany

8 ²European Centre for Medium-Range Weather Forecasts, Reading, UK

9 ³Faculty of Mathematics and Physics, University of Ljubljana, Ljubljana, Slovenia

10 **Key Points:**

- 11 • A new method decomposes divergence due to the Kelvin, MRG, inertia-gravity
12 (IG) and Rossby waves in terms of the zonal scales
13 • Up to about 6% of the zonally-integrated divergence power in the tropical UTLS
14 in August 2018 in ERA5 is attributed to Kelvin and MRG waves
15 • Partitioning of the stratospheric divergence, almost entirely in IG waves, depends
16 on the background flow

Corresponding author: Valentino Neduhal, valentino.neduhal@uni-hamburg.de

17 **Abstract**

18 The paper presents a new method for the decomposition of the horizontal wind diver-
 19 gence among the linear wave solutions on the sphere: inertia-gravity (IG), mixed Rossby-
 20 gravity (MRG), Kelvin and Rossby waves. The work is motivated by the need to quan-
 21 tify the vertical velocity and momentum fluxes in the tropics where the distinction be-
 22 tween the Rossby and gravity regime, present in the extratropics, becomes obliterated.
 23 The new method decomposes divergence and its power spectra as a function of latitude
 24 and pressure level. Its application on ERA5 data in August 2018 reveals that the Kelvin
 25 and MRG waves made about 6% of the total divergence power in the upper troposphere
 26 within 10⁰S-10⁰N, that is about 25% of divergence. Their contribution at individual zonal
 27 wavenumbers k can be much larger; for example, Kelvin waves made up to 24% of di-
 28 vergence power at synoptic k in August 2018. The relatively small roles of the Kelvin
 29 and MRG waves in tropical divergence power are explained by decomposing their kinetic
 30 energies into rotational and divergent parts. The Rossby wave divergence power is 0.3-
 31 0.4% at most, implying up to 6% of global divergence due to the beta effect. The remain-
 32 ing divergence is about equipartitioned between the eastward- and westward-propagating
 33 IG modes in the upper troposphere, whereas the stratospheric partitioning depends on
 34 the background zonal flow. This work is a step towards a unified decomposition of the
 35 momentum fluxes that supports the coexistence of different wave species in the tropics
 36 in the same frequency and wavenumber bands.

37 **Plain Language Summary**

38 The atmosphere is commonly understood in terms of linear waves such as the large-
 39 scale, low-frequency and quasi-rotational Rossby waves and small-scale, high-frequency
 40 and quasi-divergent inertia-gravity (IG) waves. In extratropics, IG waves are commonly
 41 analysed in terms of the horizontal wind divergence. The same approach does not work
 42 in the tropics, where the Kelvin waves and mixed Rossby-gravity (MRG) waves hinder
 43 the frequency and scale separation as well as the separation between the vorticity and
 44 divergence. As a consequence, an assumption of a single wave type inhabiting a band
 45 of scales and frequencies is commonly made. We developed a method for the decompo-
 46 sition of divergence that does not require this assumption. By applying the new method
 47 to the ERA5 data in August 2018, we quantified the divergence power of each wave type
 48 at various pressure levels, latitude bands and zonal scales. Our results reveal that in Au-
 49 gust 2018, the Kelvin and MRG wave constituted up to approximately 25% of divergence
 50 in the tropical upper troposphere and lower stratosphere (UTLS). The remaining tropi-
 51 cal divergence power is roughly evenly divided between eastward-propagating and westward-
 52 propagating IG modes in the upper troposphere whereas its partitioning in the tropi-
 53 cal stratosphere and extratropics depends on the background zonal flow. Understand-
 54 ing divergence partitioning will lead to more accurate estimates of the vertical momen-
 55 tum fluxes in the UTLS.

56 **1 Introduction**

57 The divergence of the horizontal wind is a key variable of atmospheric general cir-
 58 culation, along with the vertical component of relative vorticity. Divergent winds and
 59 associated vertical motions drive variability from diurnal (e.g., Dai & Deser, 1999) to con-
 60 vective (e.g., Banacos & Schultz, 2005) and interannual and decadal time scales (e.g.,
 61 Zurita-Gotor, 2019, 2021). Large-scale precipitation is often considered as a part of di-
 62 vergent circulation collocated with the maximal convergence such as monsoon (e.g., Tren-
 63 berth et al., 2000) or the inter-tropical convergence zone (ITCZ; e.g., Berry & Reeder,
 64 2014).

65 However, divergence remains uncertain, especially in the tropics where its ampli-
 66 tude relative to vorticity is largest. Divergence is the first order derivative of the wind

67 and its accuracy is at best just as good as the wind observations. Large ocean areas of
 68 the tropics and the southern hemisphere are poorly covered by wind observations, leav-
 69 ing the accuracy of divergent processes in these regions in reanalysis data to a large ex-
 70 tent constrained by temperature information (i.e. satellite radiances), and model and
 71 data assimilation properties.

72 Indirect observations of the divergence field are possible using the Gauss’s theo-
 73 rem applied to dropsondes distributed along circular flight patterns (Bony & Stevens,
 74 2019, and references therein), an approach applied in the NARVAL2 (Bony & Stevens,
 75 2019) and EUREC⁴A (Bony et al., 2017) campaigns in the tropical Atlantic. While lo-
 76 cal and rare, such observations validate the divergence simulated by the km-scale mod-
 77 els, in addition to elucidating process understanding. The comparison of the observed
 78 wind profiles during EUREC⁴A with the model of the European Centre for Medium-Range
 79 Weather Forecasts (ECMWF) showed that the structure and variability of the trade winds
 80 are reasonably well reproduced by the model, although biases remain (Savazzi et al., 2022).
 81 Recently concluded Aeolus mission carrying the first Doppler wind lidar in space (Stoffelen
 82 et al., 2005) provided almost four years of global wind profiles that led to analysis and
 83 forecast improvements in all numerical weather prediction (NWP) systems that assim-
 84 ilated Aeolus winds (e.g., Rennie et al., 2021). The intercomparison of Aeolus data also
 85 quantified model biases in the upper tropical troposphere and lower stratosphere (UTLS)
 86 (Bley et al., 2022). However, the spatio-temporal scarcity and short duration of the Ae-
 87 olus mission do not allow quantification of uncertainties in atmospheric divergence in weather
 88 and climate models. Consequently, divergence, or associated velocity potential, provided
 89 by (re)analyses is commonly used as a proxy of truth when analysing phenomena with
 90 significant vertical motions, from the large-scale flows such as the Walker circulation (e.g.,
 91 Wang, 2002) to the organisation of convection and gravity wave dynamics (e.g., Uccellini
 92 & Koch, 1987). In fact, divergence is a common proxy of gravity or inertia-gravity (IG)
 93 waves (e.g., Waite & Snyder, 2009; Dörnbrack et al., 2022).

94 The spectrum of the kinetic energy associated with the divergent part of the hor-
 95 izontal circulation (i.e. the divergent kinetic energy as given by the Helmholtz decom-
 96 position) is one way to study gravity wave energetics (e.g., Waite & Snyder, 2009). This
 97 works well in extratropics thanks to large differences between the phase speeds and hor-
 98 izontal scales of the Rossby waves and gravity waves. The same approach breaks down
 99 near the equator where the Kelvin waves and the mixed Rossby-gravity (MRG) waves
 100 fill the frequency gap between the Rossby and gravity waves. Furthermore, tropical IG
 101 waves can have large scales and low frequency. Contributions of these non-Rossby waves
 102 (i.e. of the IG, MRG, and Kelvin waves) to the overall tropical divergence has not yet
 103 been performed. It is carried out in this paper which shows how divergence associated
 104 with the Kelvin, MRG and other waves vary with the zonal wavenumber, latitude and
 105 pressure level.

106 The NWP models and reanalysis systems which have dynamical cores based on the
 107 spherical harmonics as basis functions have divergence as a prognostic variable, for ex-
 108 ample, the ECMWF IFS model (e.g., Wedi, 2014). However, the spherical harmonics are
 109 eigensolutions of the linearised barotropic vorticity equation and are not informative about
 110 the tropical wave motions that are defined as eigensolutions of the linearised primitive
 111 equations on the sphere or on the equatorial beta plane (e.g., Matsuno, 1966; Gill, 1980;
 112 Kiladis et al., 2009; Webster, 2020). At small scales in the tropics, IG waves can be treated
 113 in the same way as in the midlatitudes, i.e. using the Boussinesq approximation and ne-
 114 glecting effects of rotation (e.g., Nappo, 2002). At synoptic and larger scales, the Kelvin
 115 waves and the MRG waves become major contributors to the total non-Rossby wave vari-
 116 ance spectra (Žagar et al., 2009a). The quantification of contributions of different wave
 117 species to the vertical momentum fluxes has so far assigned bands of wavenumbers and
 118 frequencies to a single wave type per band (e.g., Kim & Chun, 2015; Ern & Preusse, 2009).
 119 The work presented in this paper supports the presence of multiple waves in the same

120 wavenumbers and frequency bands, a step towards a more realistic decomposition of the
 121 momentum fluxes driving the tropical middle atmosphere variability.

122 In what follows, we derive a unified method for the decomposition of divergence
 123 associated with the Kelvin, MRG, and IG waves, in addition to the Rossby waves. The
 124 method is spherical and provides the latitude-by-latitude and level-by-level divergence
 125 zonal wavenumber power spectra partitioned among the wave species. As stated above,
 126 we refer to the Kelvin, MRG, and IG waves, including their zonal-mean state (the zonal
 127 wavenumber $k = 0$), as the non-Rossby modes. As the Kelvin and MRG waves are equa-
 128 torially trapped, the non-Rossby and IG modes are basically the same in the middle and
 129 high latitudes. Details of the method and its validation are provided in Section 2. Re-
 130 sults of the method application to ERA5 reanalyses in August 2018 are presented in Sec-
 131 tion 3. Discussion, conclusions, and outlook are given in Section 4.

132 2 Decomposition of the horizontal wind divergence on the sphere

133 The decomposition of the horizontal wind divergence denoted \mathcal{D} , is derived using
 134 the normal-mode function (NMF) framework. The NMFs are the eigensolutions of the
 135 linearised primitive equations around the state of rest and they are defined as a prod-
 136 uct of the Hough harmonics and the vertical structure functions (VSFs) (e.g., Kasahara,
 137 2020). First, the NMF decomposition is summarized in order to introduce the notation
 138 and variables. This is followed by the derivation of divergence and its zonal wavenum-
 139 ber spectra and the method validation.

140 2.1 The horizontal wind divergence in the NMF framework

141 The computation of divergence is carried out in the system with the pressure ver-
 142 tical coordinate. Starting from the adiabatic, hydrostatic primitive equations linearized
 143 about a motionless basic state on a flat Earth with the globally-averaged vertical tem-
 144 perature profile, one derives eigensolutions by making an assumption of separability be-
 145 tween the vertical and horizontal dependencies. In this way, the global baroclinic atmo-
 146 sphere is represented in terms of M global shallow-water equation systems. The param-
 147 eter M is defined by the number of the vertical layers used to discretize the atmosphere
 148 between the surface at pressure p_s and the top level where $p = 0$. Each shallow-water
 149 system is characterized by a mean depth, also known as the "equivalent depth", and it
 150 corresponds to one eigenvalue of the vertical structure equation (e.g., Staniforth et al.,
 151 1985). The equivalent depths couple the horizontal wind and geopotential height oscil-
 152 lations with the vertical structure functions - eigensolutions of the vertical structure equa-
 153 tion. The horizontal motions are represented by a series of Hough harmonics which are
 154 products of the Hough vector functions in the meridional direction and waves in the lon-
 155 gitudinal direction (Swarztrauber & Kasahara, 1985).

156 The 3D NMF decomposition consists of two steps. In the first step, the data vec-
 157 tor $(u, v, h)^T$ with the geopotential height (h) and two wind components (u, v) on the
 158 constant pressure levels is projected onto an orthogonal set of M vertical structure func-
 159 tions $G_m(p)$, $m = 1, \dots, M$. For a single point (λ, φ, p_j) , the projection is written as

$$160 \quad (u, v, h)^T(\lambda, \varphi, p_j) = \sum_{m=1}^M G_m(p_j) \mathbf{S}_m (u_m, v_m, h_m)^T(\lambda, \varphi) , \quad (1)$$

161 where the scaling matrix \mathbf{S}_m is a 3×3 diagonal matrix with elements $\sqrt{gD_m}$, $\sqrt{gD_m}$
 162 and D_m that make the data vector after the vertical projection, $(u_m, v_m, h_m)^T$, dimen-
 163 sionless, denoted $(\tilde{u}_m, \tilde{v}_m, \tilde{h}_m)^T$. Parameters λ and φ stand for the geographical longi-
 164 tude and latitude, respectively.

165 The non-dimensional rotating global shallow-water equations read

$$166 \quad \frac{\partial \tilde{u}_m}{\partial \tilde{t}} - \sin \varphi \tilde{v}_m + \frac{\gamma_m}{\cos \varphi} \frac{\partial \tilde{h}_m}{\partial \lambda} = 0, \quad (2a)$$

$$167 \quad \frac{\partial \tilde{v}_m}{\partial \tilde{t}} + \sin \varphi \tilde{u}_m + \gamma_m \frac{\partial \tilde{h}_m}{\partial \varphi} = 0, \quad (2b)$$

$$168 \quad \frac{\partial \tilde{h}_m}{\partial \tilde{t}} + \frac{\gamma_m}{\cos \varphi} \left(\frac{\partial \tilde{u}_m}{\partial \lambda} + \frac{\partial}{\partial \varphi} (\tilde{v}_m \cos \varphi) \right) = 0, \quad (2c)$$

169 where γ_m is a dimensionless parameter defined as $\gamma_m = \sqrt{gD_m}/(2a\Omega)$, with parameters D_m , a , Ω and g denoting the equivalent depth of the m -th vertical mode, the Earth radius, rotation rate, and gravity, respectively. The parameter γ_m is the inverse of the square of the Lamb's parameter which characterizes the nature of shallow-water flows (Swarztrauber & Kasahara, 1985). The discrete solutions of the system of equations (2) in terms of the Hough harmonics in space and harmonics in time can be written as

$$176 \quad \begin{vmatrix} \tilde{u}_m(\lambda, \varphi, \tilde{t}) \\ \tilde{v}_m(\lambda, \varphi, \tilde{t}) \\ \tilde{h}_m(\lambda, \varphi, \tilde{t}) \end{vmatrix} = \sum_{n=1}^R \sum_{k=-K}^K \chi_n^k(m) \begin{vmatrix} U_n^k(\varphi; m) \\ iV_n^k(\varphi; m) \\ Z_n^k(\varphi; m) \end{vmatrix} e^{ik\lambda} e^{-i\tilde{\nu}_n^k(m)\tilde{t}}. \quad (3)$$

177 The complex expansion coefficient $\chi_n^k(m)$ provides a multivariate spectral representation of the global 3D circulation, with a single mode defined by a unique index (k, n, m) , with k and n defining the zonal wavenumber and the meridional mode index, respectively. For every vertical mode m in (1), the Hough harmonic \mathbf{H}_n^k is defined as $\mathbf{H}_n^k(\lambda, \varphi; m) = [U_n^k \ iV_n^k \ Z_n^k]^T(\varphi; m) e^{ik\lambda}$, where U_n^k , V_n^k and Z_n^k are the Hough functions for the zonal wind, meridional wind and the geopotential height, and the imaginary unit $i = \sqrt{-1}$ in front of V_n^k accounts for its $\pi/2$ shift with respect to U_n^k (Swarztrauber & Kasahara, 1985). The Hough functions satisfy the energy norm

$$185 \quad \int_{-1}^1 (U_p U_r + V_p V_r + Z_p Z_r) d\mu = \delta_{pr}, \quad (4)$$

186 where $\mu = \sin \varphi$, and p and r each represent a three-component modal index (k, n, m) . Individual Hough harmonics \mathbf{H}_n^k describe the horizontal structure of a single mode with $\tilde{\nu}_n^k(m)$ being the corresponding dimensionless frequency of that mode.

189 The mode index n includes 3 wave species: the westward-propagating Rossby modes and the eastward- and westward-propagating inertia-gravity modes, denoted EIG and WIG, respectively. Thus, the maximal number of meridional modes in (3), R , combines N_R Rossby modes including the mixed Rossby-gravity mode as the lowest meridional mode ($n = 0$) solution, N_{EIG} eastward-propagating inertia-gravity (EIG) modes, including the Kelvin waves as the lowest meridional mode ($n = 0$), and N_{WIG} westward-propagating inertia-gravity (WIG) modes; $R = N_R + N_{EIG} + N_{WIG}$. This particular choice of indexing is motivated by the wish to avoid another index going from 1 to 3 which would represent the three main wave species but would not support a separate treatment of the Kelvin and MRG modes. The notation (3) follows the NMF formulation in the MODES software (Žagar et al., 2015). Žagar et al. (2023) and references therein provides detailed discussion of the steps involved in the computation of $\chi_n^k(m)$.

202 The computations of divergence directly from the horizontal velocities expanded in terms of Hough harmonics (3) require the computation of the $\partial V_n^k / \partial \varphi$ that is not readily available but should be evaluated numerically. This makes the direct computation of divergence cumbersome. A natural way for computing \mathcal{D} is to exploit the continuity equation (2c) as performed next. For vertical mode m , the non-dimensional divergence $\tilde{\mathcal{D}}_m$ can be expressed using Eq. (2c) as:

$$208 \quad \tilde{\mathcal{D}}_m(\lambda, \varphi, \tilde{t}) = \tilde{\nabla} \cdot \tilde{\mathbf{V}} = -\frac{\partial}{\partial \tilde{t}} \tilde{h}_m(\lambda, \varphi, \tilde{t}), \quad (5)$$

209 where the non-dimensional horizontal "del" operator is given by

$$210 \quad \tilde{\nabla}_m = \frac{\gamma_m}{\cos(\varphi)} \left[\frac{\partial}{\partial \lambda}(\cdot), \frac{\partial}{\partial \varphi}(\cos(\varphi)(\cdot)) \right]. \quad (6)$$

211 The spatial structure of the geopotential height for m -th vertical mode is given by the
212 third equation in the equation set (3). Its substitution in (5) gives \tilde{D}_m as

$$213 \quad \tilde{D}_m(\lambda, \varphi, \tilde{t}) = \sum_{n=1}^R \sum_{k=-K}^K i\tilde{\nu}_n^k \chi_n^k(m) Z_n^k(\varphi) e^{ik\lambda} e^{-i\tilde{\nu}_n^k \tilde{t}}. \quad (7)$$

214 Analogous to (1), dimensional divergence at pressure level p is obtained by multiplying
215 (7) with 2Ω and summing up contributions from all VSFs. Dropping the time depen-
216 dence, divergence is defined as

$$217 \quad \mathcal{D}(\lambda, \varphi, p) = \sum_{m=1}^M \sum_{n=1}^R \sum_{k=-K}^K i2\Omega \tilde{\nu}_n^k(m) \chi_n^k(m) Z_n^k(\varphi; m) G_m(p) e^{ik\lambda}. \quad (8)$$

218 The major advantage of Eq. (8) is that \mathcal{D} is obtained by a simple multiplication
219 and summation over readily available VSFs and the Hough functions. All input coeffi-
220 cients and functions required in (8) are available after the expansion of 3D data such as
221 using MODES. The divergence associated with the Rossby, IG, MRG, or Kelvin waves
222 is obtained by limiting the summation to a subset of n associated with the modes of in-
223 terest. Similarly, filtering in terms of the zonal wavenumbers is trivial. Žagar et al. (2023)
224 make use of Eq. (8) in the derivation of the pressure vertical velocity ω and its kinetic
225 energy spectra in the hydrostatic atmosphere.

226 Equation (8) states that divergence \mathcal{D} has a phase shift of $\pi/2$ with respect to the
227 geopotential height h . This is illustrated in Fig. 1 for several modes with the zonal wavenum-
228 ber $k = 1$. For the eastward-propagating Kelvin and $n = 1$ EIG mode ($\nu > 0$), and
229 for the westward-propagating $n = 1$ Rossby, $n = 0$ and $n = 1$ WIG and MRG waves
230 ($\nu < 0$), divergence lags the geopotential height for the quarter of a cycle. The $\pi/2$ shift
231 between the geopotential and divergence is an important universal property well known
232 from the quasi-geostrophic theory for the Rossby waves (e.g., Holton, 2004), and from
233 the polarization equations coupling the pressure, temperature, and velocity perturba-
234 tions for internal gravity waves (e.g., Nappo, 2002). The same phase shift applies to the
235 vertical velocity as \mathcal{D} and ω are always in phase (Žagar et al., 2023).

236 2.2 Computation of the divergence power spectrum

237 An advantage of computing divergence in Hough harmonics space is the ease with
238 which the associated zonal wavenumber power spectra can be computed. The Fourier
239 expansion of divergence along the latitude circle is

$$240 \quad \mathcal{D}(\lambda, \varphi, p) = \sum_{k=-K}^K \hat{\mathcal{D}}_k(\varphi, p) e^{ik\lambda}, \quad (9)$$

241 which combined with Eq. (8) gives the definition of the Fourier expansion coefficient $\hat{\mathcal{D}}_k$
242 as

$$243 \quad \hat{\mathcal{D}}_k(\varphi, p) = \sum_{m=1}^M \sum_{n=1}^R i2\Omega \tilde{\nu}_n^k(m) \chi_n^k(m) Z_n^k(\varphi; m) G_m(p). \quad (10)$$

244 The Parseval theorem provides the total power of divergence on pressure level p along
245 the latitude circle φ :

$$246 \quad \frac{1}{2\pi} \int_0^{2\pi} \mathcal{D}^2 d\lambda = \sum_{k=-K}^K \hat{\mathcal{D}}_k [\hat{\mathcal{D}}_k]^* = \sum_{k=0}^K (2 - \delta_{k0}) \left| \hat{\mathcal{D}}_k \right|^2 = \sum_{k=0}^K E_D^k(\varphi, p) = E_D(\varphi, p), \quad (11)$$

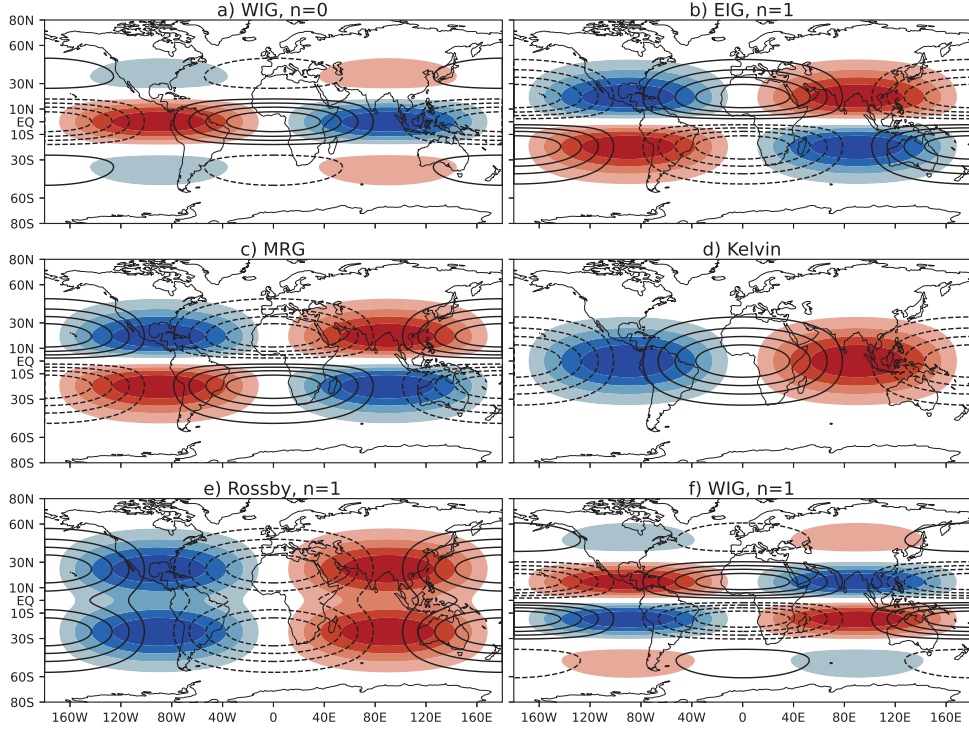


Figure 1. The horizontal structure of the geopotential height (colors) and divergence (iso-lines) for a) $n = 0$ westward inertia-gravity (WIG), b) $n = 1$ eastward inertia-gravity (EIG), c) mixed Rossby-gravity (MRG), d) Kelvin, e) $n = 1$ Rossby and f) $n = 1$ WIG mode for zonal wavenumber $k = 1$ and equivalent depth $D = 1015$ m. Blue colors and dashed lines denote negative geopotential height and convergence, respectively. Every field is normalized by its maximal values and the $[-1, 1]$ interval is shown with 0.2 spacing.

247 where $\delta_{k0} = 1$ for $k = 0$ and 0 otherwise (with \hat{D}_k presented only for $k > 0$). A single
 248 latitude circle divergence power spectra can be integrated meridionally on the Gaus-
 249 sian latitude grid used for the Hough harmonics expansion. For the latitude belt $[\varphi_1, \varphi_2]$,
 250 the total divergence power in zonal wavenumber k is

$$251 \quad E_D^k(p) = \int_{\varphi_1}^{\varphi_2} E_D^k(\varphi, p) \cos \varphi \, d\varphi \bigg/ \int_{\varphi_1}^{\varphi_2} \cos \varphi \, d\varphi \quad (12)$$

252 For $\varphi_1 = -\pi/2$ and $\varphi_2 = \pi/2$, we obtain the globally integrated divergence power spec-
 253 trum $E_D^k(p)$. An example is shown in Fig. 2 for the global spectra averaged over strato-
 254 spheric levels of ERA5 between 1 and 10 hPa and for the levels between 100 and 1000 hPa.

255 The global divergence power spectra can be compared with the divergent kinetic
 256 energy of the horizontal wind (denoted E_{HD}) for the same dataset in Fig. 2 in order to
 257 highlight differences between the two types of spectra. The E_{HD} spectra as a function
 258 of the zonal wavenumber are computed by the spherical harmonics decomposition (e.g.,
 259 Lambert, 1984; Adams & Swartztrauber, 2001) as

$$260 \quad E_H^k = \frac{1}{4} \sum_{l=k}^N (2 - \delta_{k0}) \frac{a^2}{l(l+1)} \left(|\hat{\zeta}_{l,k}|^2 + |\hat{\delta}_{l,k}|^2 \right) = E_{HR}^k + E_{HD}^k, \quad (13)$$

261 where l is the total wavenumber, N is the global truncation and $\hat{\zeta}_{l,k}$ and $\hat{\delta}_{l,k}$ are wave
 262 components of vorticity and divergence, respectively. The rotational (E_{HR}^k) and diver-
 263 gent (E_{HD}^k) kinetic energy spectra are widely used to compare kinetic energy distribu-
 264 tions of weather and climate models with expected theoretical power laws and observa-
 265 tions (e.g., Burgess et al., 2013; Skamarock et al., 2014; Wedi, 2014). Note that E_H^k spec-
 266 tra are usually presented in terms of the total wavenumber l , meaning that contributions
 267 from all $-l < k < l$ are included in the summation of energy in single l . A comple-
 268 mentary way defined by Eq. (13) sums up all l contributing to a single zonal wavenum-
 269 ber in a triangular truncation decomposition. The summation involves weighted diver-
 270 gence expansion coefficients $\hat{\delta}_{l,k}$ by a factor $l(l+1)$ which comes from the spherical Lapla-
 271 cian of the meridional expansion in terms of the Legendre polynomials and the use of
 272 the Helmholtz decomposition (Adams & Swarztrauber, 2001).

273 The E_D^k and E_{HD}^k spectra are quantitatively and qualitatively different as seen in
 274 Fig. 2; they have different physical units and amplitudes and exhibit different spectral
 275 slopes and peaks. The E_D^k spectra describe the variance distribution of divergence \mathcal{D} in
 276 a signal processing sense. The power peak at wavenumber k implies k with a dominant
 277 amplitude in the divergence field. In contrast, the E_{HD}^k spectra are not informative about
 278 the relative distribution of divergence in terms of k . More important, the Hough har-
 279 monics decomposition provides latitude-by-latitude spectra that shows anisotropy of spher-
 280 ical divergence, besides the wave decomposition.

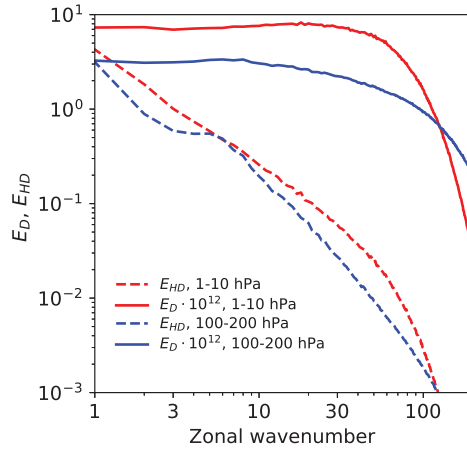


Figure 2. The divergent component of the horizontal kinetic energy spectra E_{HD}^k (in $\text{m}^2 \text{s}^{-2}$) computed using the spherical harmonic decomposition of the horizontal winds and globally integrated divergence power spectra E_D^k (in s^{-2}). Input data are ERA5 analyses in August 2018. The divergence power spectra are multiplied by 10^{12} .

281 The contributions of various wave species to the total divergence power at differ-
 282 ent wavenumbers can be quantified by taking the ratio between the spectral power $E_D^k(i)$
 283 of wave species i with the sum of the powers of all five wave species at the same k :

$$284 \quad R^k(i) = \frac{E_D^k(i)}{\sum_j E_D^k(j)}, \quad (14)$$

285 where $j = R, EIG, WIG, K, MRG$ and Rossby, Kelvin and MRG modes are denoted
 286 R, K and MRG respectively. Note that the contributions of various wave species to E_D^k

287 are not additive, in contrast to modal components of the mechanical energy that is derived
 288 using the energy norm (4) (Kasahara, 2020). The purpose of definition (14) is that
 289 the sum of individual contributions to the total divergent power is 1. Equation (14) thus
 290 provides a qualitative measure of how much various wave species contribute to the total
 291 divergence power. We checked that the effect of replacing the denominator of (14)
 292 by the total divergence E_D^k is not large (not shown).

293 Equation (10) suggests that the divergence power spectrum is proportional to the
 294 square of modal frequency $\nu(k, n, m)$, $E_D^k \propto [\nu_n^k(m)]^2$, that is, that the shapes of di-
 295 vergence power spectra for different waves are coupled to their dispersion relationships.
 296 Figure 3 shows the non-dimensional modal frequencies as a function of the zonal wavenum-
 297 ber for three equivalent depths and several meridional modes. It can be seen that the
 298 frequencies of the IG modes with small n get less dependent on k as the equivalent depth
 299 decreases. Frequency dependencies on k of different waves are discussed in Žagar et al.
 300 (2023) for the sphere, midlatitude and equatorial β planes. For the Kelvin and IG modes
 301 $\nu \propto k$, whereas for the Rossby and MRG modes $\nu \propto k^{-1}$. This implies much steeper
 302 divergence power zonal wavenumber spectra for the Rossby and MRG waves as can be
 303 expected given their rotational nature.

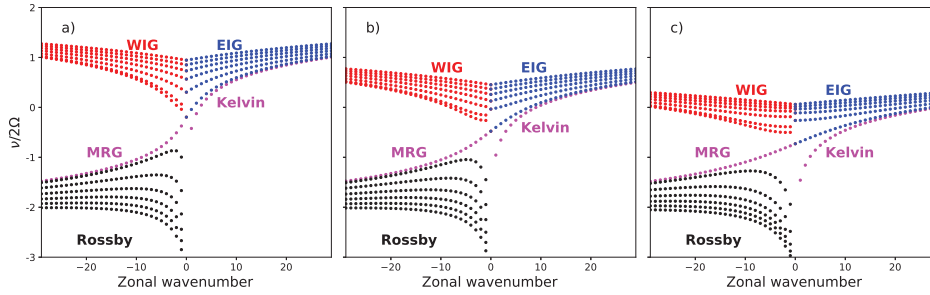


Figure 3. Frequencies of the normal modes for equivalent depths of approximately a) $D = 10$ km, b) $D = 1$ km, and c) $D = 100$ m. Frequencies are normalized by 2Ω and shown in a logarithmic scale. Frequencies of the eastward propagating inertia-gravity (EIG) are shown for the meridional indices $n = 1, 5, 10, 15, 20, 25$, where $n = 0$ EIG modes are Kelvin waves. Frequencies of the westward propagating inertia-gravity (WIG) are shown for the meridional indices $n = 0, 1, 5, 10, 15, 20, 25$ while Rossby modes are shown for the meridional indices $n = 1, 5, 10, 15, 20, 25$, where $n = 0$ Rossby modes are mixed Rossby-gravity (MRG) waves.

304 2.3 Data

305 The above described computation of the horizontal divergence in the pressure sys-
 306 tem is implemented in the MODES software (Žagar et al., 2015). The new module can
 307 be executed in a self-standing mode including scale-selected filtering of divergence in phys-
 308 ical space. It is also a part of the procedure for the computation of the pressure verti-
 309 cal velocity as well as the vertical momentum fluxes.

310 As input fields, we are using ERA5 data (Hersbach et al., 2020). The IFS model,
 311 which is used to produce ERA5, has a ‘sponge layer’ near the model top to prevent spu-
 312 rious wave reflection. This sponge layer is scale-selective and directly damps divergence.
 313 The sponge layer is represented by adding a fourth-order hyper-diffusion (∇^4) to the prog-
 314 nostic equations for vorticity, divergence and temperature fields above 10 hPa to damp

315 vertically propagating waves with an e-folding time on a given total wavenumber l of

$$316 \left(\frac{L_{max}(L_{max} + 1)}{l(l + 1)} \right)^2 \frac{\tau_H}{1 + 7.5(3 - \log(p))},$$

317 where L_{max} is the maximum total wavenumber 639 for ERA5, p is pressure in Pa, and
 318 τ_H is a timescale of 4320 s (1.2 hours). This hyper-diffusion is quite weak and has a small
 319 impact on the resolved waves. In addition, a first-order diffusion (∇) is applied on the
 320 divergence field above 1 hPa with an e-folding time on a given total wavenumber l of

$$321 \sqrt{\frac{L_{max}(L_{max} + 1)}{l(l + 1)} \frac{\tau_H}{16 - lev}},$$

322 where $lev = 1, \dots, 15$ is a vertical level index with $lev = 15$ corresponding to 1 hPa and
 323 $lev = 1$ corresponding to the model top. This diffusion is very strong and very effective
 324 at damping all resolved waves. Therefore, any analysis of divergence in the meso-
 325 sphere, above 1 hPa, will be dominated by the spurious sponge effects and should be in-
 326 terpreted with caution. The detrimental impact of the IFS sponge layer on resolved gravi-
 327 ty waves has been discussed by Gisinger et al. (2022) and Gupta et al. (2021).

328 At a horizontal grid spacing of about 30 km, with added effects from grid-scale hyper-
 329 diffusion, ERA5 skilfully resolves waves with a horizontal wavelength longer than about
 330 200 km outside the sponge layer and parametrizes the rest. The unresolved part of the
 331 gravity wave spectrum is parameterized using the Lott and Miller (1997) scheme for oro-
 332 graphic waves and the Orr et al. (2010) scheme for the non-orographic GWs. Moreover,
 333 the vertical diffusion parametrization, represented by the eddy-diffusivity mass-flux frame-
 334 work, acts in the stratosphere in ERA5.

335 The input data are defined on the 137 model levels. The list of levels can be seen
 336 at <https://confluence.ecmwf.int/display/UDOC/L137+model+level+definitions>.
 337 In order to keep the vertical resolution of the reanalysis data, the wind components and
 338 model-level geopotential are interpolated from the hybrid sigma-pressure levels to pres-
 339 sure levels corresponding to the globally averaged pressure of the full model levels. The
 340 interpolation method follows the method implemented in the ECMWF IFS system. The
 341 horizontal grid is a regular N320 Gaussian grid with 1280×640 points along the latitude
 342 circle and pole to pole, respectively, corresponding to a resolution of 31 km at the equa-
 343 tor. The regular Gaussian grid data are extracted directly from the ECMWF MARS database
 344 (C3S, 2017) using the MIR interpolation procedure. For validating purposes, we anal-
 345 ysed a few dates in August 2016 during the NARVAL campaign. The main dataset is
 346 for August 2018 that was used in Žagar et al. (2023) making possible a comparison be-
 347 tween the spectra of the vertical kinetic energy and divergence.

348 The truncations used in MODES are $K = 350$ zonal wavenumbers, $R = 600$ merid-
 349 ional modes including $N_R = N_{EIG} = N_{WIG} = 200$ and $M = 60$ vertical modes. As
 350 the number of vertical modes is less than half of the number of levels, we expect signif-
 351 icant deviations in \mathcal{D} reconstructed by MODES from the divergence field extracted di-
 352 rectly from ERA5. The reason for using a smaller number of vertical modes is a fast de-
 353 crease in the equivalent depth that leads to equatorially-trapped horizontal structures
 354 (Žagar et al., 2009b). However, differences in the upper troposphere and in the middle
 355 atmosphere, which are the focus of our discussion, are not large or detrimental to the
 356 study. Except for a high-resolution NMF decomposition by Terasaki et al. (2011) that
 357 provided global energy spectra including 750 zonal wavenumbers, this is the highest res-
 358 olution data analysed to date with MODES.

359 2.4 Method validation

360 Figure 4 compares divergence in ERA5 with its modal reconstruction \mathcal{D} over the
 361 tropical Atlantic on 19 August 2016. The ERA model-level divergence is interpolated

362 to the same pressure levels as used in MODES. We picked a weather-rich day of 19 Au-
 363 gust with tropical storm Fiona (Kimberlain, 2016) as the hardest test for the method.
 364 The divergence associated with the storm can be seen near 18°N, 43°W throughout the
 365 troposphere. Modal \mathcal{D} resembles ERA5 very well. Differences in the vertical cross-section
 366 through the troposphere are expected due to the vertical truncation. Detailed statisti-
 367 cal evaluation of differences confirms that differences start below the level where the ver-
 368 tical decomposition is no longer complete (not shown).

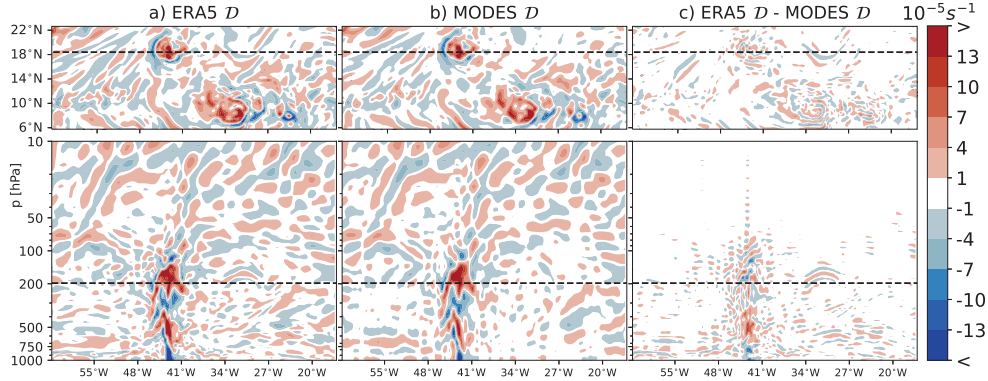


Figure 4. a) ERA5 divergence, b) divergence reconstructed by MODES and c) ERA5–MODES, at 10 UTC on 19 August 2016 at 197 hPa (top row), and the vertical cross-section along 18.4°N (bottom row). The dashed line in the top row is along 18.4°N and the dashed line in the bottom row indicates 197 hPa level.

369 In Fig. 5 the total divergence signal at 10 UTC on 19 August 2016 is decomposed
 370 into components and presented for the global domain at 150 hPa level. Although sev-
 371 eral panels in this figure appear very similar, this is the first example of the systematic
 372 decomposition of divergence and all components are presented for completeness. First,
 373 the total divergence \mathcal{D} is separated into Rossby modes (\mathcal{D}_R) and non-Rossby modes (\mathcal{D}_{nR}),
 374 $\mathcal{D} = \mathcal{D}_R + \mathcal{D}_{nR}$. Then, \mathcal{D}_{nR} is partitioned in terms of the IG modes (\mathcal{D}_{IG}), Kelvin modes
 375 (\mathcal{D}_K) and MRG modes (\mathcal{D}_{MRG}), $\mathcal{D}_{nR} = \mathcal{D}_{IG} + \mathcal{D}_K + \mathcal{D}_{MRG}$. Finally, IG modes are
 376 split into WIG and EIG parts, $\mathcal{D}_{IG} = \mathcal{D}_{EIG} + \mathcal{D}_{WIG}$. First of all, Fig. 5 shows that
 377 the global divergence is dominated by small scales and it nearly completely projects onto
 378 the IG modes. The WIG modes dominate in the extratropics where \mathcal{D}_{WIG} is due to ageostrophic
 379 circulation associated with baroclinic Rossby waves superimposed on the mean westerly
 380 flow, especially in the Southern Hemisphere (SH) that has winter season (Fig. 5h). The
 381 divergence due to the linear Rossby waves is the geostrophic wind divergence on the sphere
 382 which is proportional to $v_g \beta / f$, has a small amplitude and a large-scale structure (Fig. 5b).

383 Focusing now on the tropics, we can notice a local maximum of the divergence in
 384 \mathcal{D}_{IG} , \mathcal{D}_{EIG} , and \mathcal{D}_{WIG} due to the tropical storm Fiona discussed in Fig. 4. This is be-
 385 cause the flow in cyclostrophic balance, typical for tropical cyclones (e.g., Jakobsen &
 386 Madsen, 2004), will in linear decomposition project partly on Rossby and partly on IG
 387 modes. Local maxima and minima in \mathcal{D}_{IG} can be spotted along the inter-tropical con-
 388 vergence zone and in the monsoon-affected areas of South-East Asia and western Pacific,
 389 but also over the topographic gravity wave hot spot over the Andes, Himalayas, and the
 390 mid-west USA. The Kelvin wave divergence is centered at the equator and an order of
 391 magnitude smaller than \mathcal{D}_{IG} with the largest scale and amplitudes over the Indian Ocean
 392 and West Pacific (Fig. 5d). In contrast, the MRG divergence, \mathcal{D}_{MRG} (Fig. 5e), has a smaller
 393 amplitude and larger scales, similar to \mathcal{D}_R . Note also that $\mathcal{D}_{MRG} = 0$ at the equator

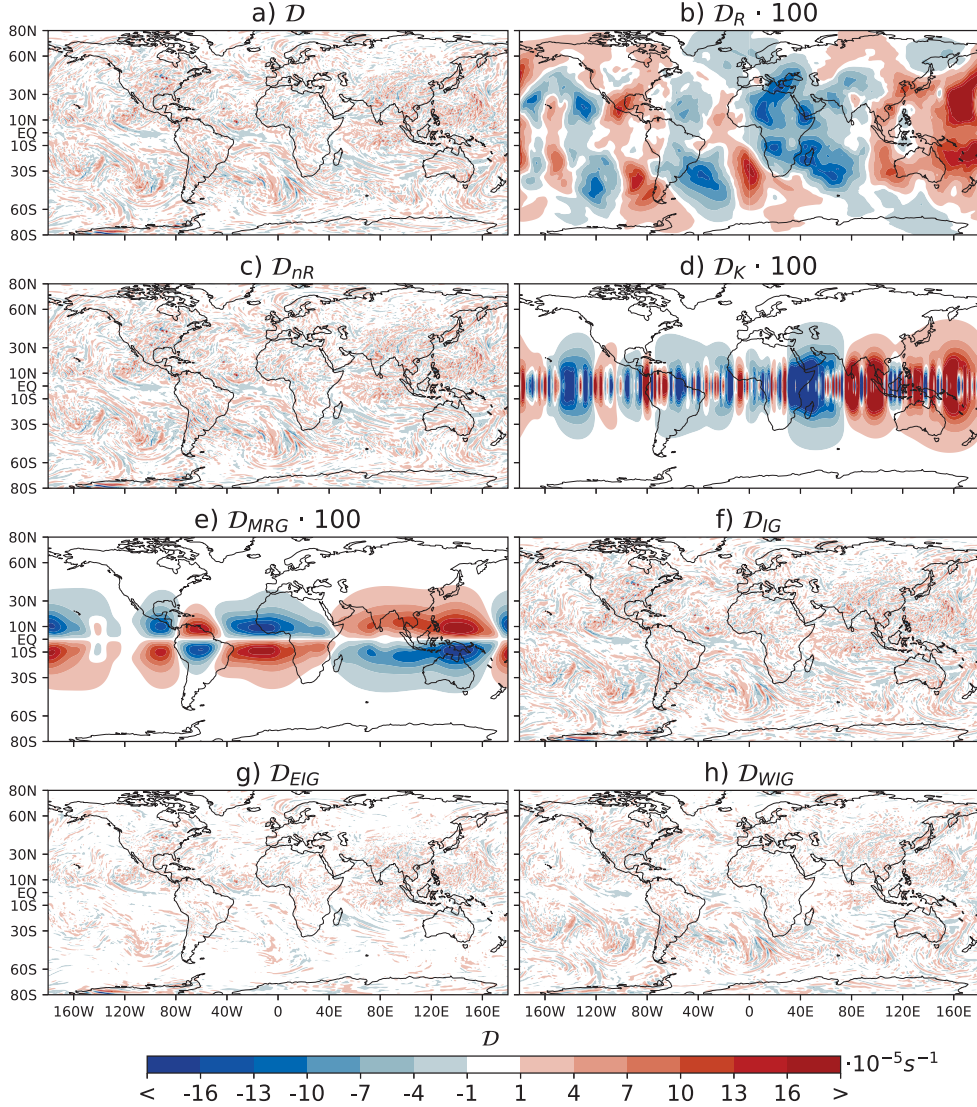


Figure 5. Total divergence \mathcal{D} , decomposed into the Rossby, \mathcal{D}_R , and non-Rossby, \mathcal{D}_{nR} , parts. The non-Rossby divergence is a sum of the Kelvin, \mathcal{D}_K , MRG, \mathcal{D}_M , and IG, \mathcal{D}_G , components, with \mathcal{D}_G made of the EIG, \mathcal{D}_{EG} , and WIG, \mathcal{D}_{WG} , parts. The decomposition is applied to ERA5 circulation at the level near 150 hPa on 19 August 2016, 10 UTC. The Rossby, Kelvin and MRG parts are multiplied by 100.

394 where its zonal wind is zero and the meridional wind is strongest. This implies that the
 395 vertical velocity and the vertical momentum fluxes of the MRG waves are also zero at
 396 the equator and likely to maximise within $5^\circ - 10^\circ$ degrees away from the equator.

397 Further comparison of divergence profiles over the NARVAL campaign region with
 398 \mathcal{D} shows that ERA5 lacks many details in the vertical divergence profile and further de-
 399 tails are missed by our incomplete reconstructions in the lower troposphere, although
 400 the main features and amplitude of the divergence profiles are represented reasonably

401 well. The \mathcal{D} decomposition into components shows that the divergence is completely in
 402 the \mathcal{D}_{IG} component as expected (not shown).

403 3 Modal decomposition of divergence in August 2018

404 Now we present level-by-level divergence power spectra in August 2018 for differ-
 405 ent latitude belts focusing on the upper troposphere and the middle atmosphere. The
 406 period was characterised by easterly zonal winds in the tropical stratosphere between
 407 the tropopause and about 20 hPa, i.e. the easterly phase of the Quasi-Biennial-Oscillation
 408 (QBO, e.g., Baldwin et al. (2001)) with strongest mean-zonal winds of about 50 m/s near
 409 30 hPa. The strongest westerlies around 30 m/s were near 15 hPa, and easterlies were
 410 present above 5 hPa. The rest of the zonal mean flow was typical for this period of the
 411 year: prevalent weak easterlies in the tropical troposphere, westerlies in the SH, subtrop-
 412 ics and middle latitudes, and a polar night jet in the middle atmosphere of SH high lat-
 413 itudes.

414 Even though we are primarily interested in the quantification of tropical divergence,
 415 it is worth presenting global properties of divergence spectra partitioned into the Rossby
 416 and non-Rossby parts as the first application of the new method. The results are split
 417 between the tropical, subtropical, midlatitude and high latitude belts for levels above
 418 500 hPa. First, we discuss E_D^k in the middle and high latitudes, then the tropical spec-
 419 tra presented for every level after averaging over 31 samples. The shortest analysed scales
 420 appear noisy, most likely because of a short dataset. A longer dataset and the whole ERA5
 421 periods are planned for the future work along with introducing the non-linear normal-
 422 mode decomposition to differentiate between slowly evolving IG modes slaved to the Rossby
 423 mode dynamics and faster IG modes including internal gravity waves (e.g., Ko et al., 1981;
 424 Tribbia, 2020).

425 3.1 Middle and high latitudes

426 Figure 6 and Figure 7 present the divergence power spectra E_D^k averaged over lat-
 427 itudes within $30^\circ-60^\circ$ and $60^\circ-80^\circ$ in both hemispheres, respectively. The Rossby E_D^k
 428 is multiplied by 100 in order to be visualised using the same colorbar as other compo-
 429 nents.

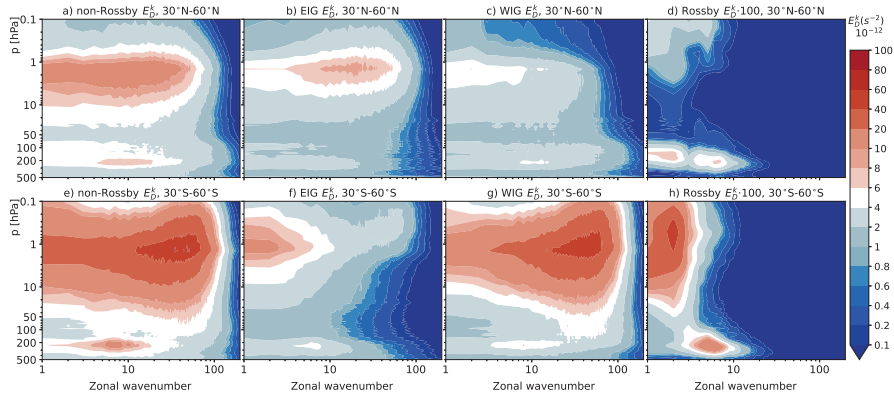


Figure 6. Level-by-level (a,e) non-Rossby, (b,f) EIG, (c,g) WIG and (d,h) Rossby mode divergence power spectra E_D^k averaged for latitude belts (a-d) $30^\circ\text{N}-60^\circ\text{N}$ and (e-h) $30^\circ\text{S}-60^\circ\text{S}$ for August 2018. The extratropical non-Rossby spectra correspond to the sum of WIG and EIG spectra. The Rossby spectra are multiplied by 100. Note the nonlinear contour intervals.

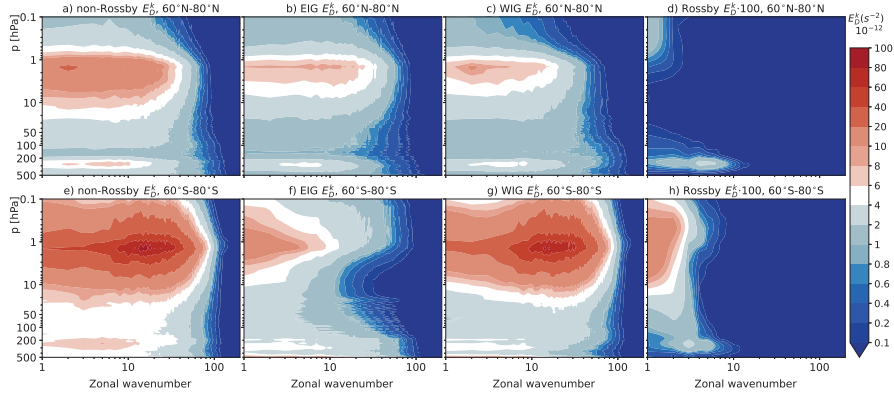


Figure 7. As in Fig. 7 but for (a-d) 60°N–80°N and (e-h) 60°S–80°S.

430 A prominent feature of the two figures is the maximum in stratospheric E_D^k near
 431 1 hPa at subsynoptic scales of IG modes. While present in both hemispheres, it is pre-
 432 dominantly in the WIG divergent spectra of the winter hemisphere (SH), with the max-
 433 imum at $k \approx 50$. The maximal E_D^k in the Northern Hemisphere (NH) is smaller and
 434 shifted to larger scale compared to the SH.

435 The E_D^k maximum near 1 hPa is due to the artificial sponge layer in ERA5, which
 436 very strongly damps divergence from 1 hPa upwards (see section 2.3) and therefore leads
 437 to all gravity waves depositing their momentum at or near the 1 hPa level (see e.g., Fig.
 438 2c in Gupta et al. (2021)). If the sponge layer was absent, the maximum would be lo-
 439 cated at a much higher altitude, at a natural breaking/saturation level of gravity waves
 440 (cf. Fig. 2c to Fig. 2d in Gupta et al. (2021)). A decrease in the divergence power of IG
 441 modes for $k > 100$ is due to the insufficient resolution of the ERA5 data. In IFS model
 442 simulations at higher horizontal resolution than ERA5, the small-scale gravity waves with
 443 $k > 100$ play an increasingly important role in the momentum budget (Figs. 2 and 3
 444 in Polichtchouk et al. (2023)).

445 The majority of mesoscale E_D^k in WIG modes in extratropical winter hemisphere
 446 (SH) can be understood by vertically-propagating IG waves filtered by the westerly flow
 447 of the stratospheric polar vortex (Fig. 6g and Fig. 7g). Such features can be seen in the
 448 real-time decomposition of the ECMWF forecasts on the MODES webpage, [https://
 449 modes.cen.uni-hamburg.de/products#POL](https://modes.cen.uni-hamburg.de/products#POL). A significant level of divergence power at
 450 planetary scales in panels e), f), and g) of Figs 6-7 is most likely due to the linear mode
 451 decomposition. The linear balance decomposition of the polar vortex, which is charac-
 452 terised by the gradient wind balance, partially projects the vortex onto the planetary-
 453 scale IG modes, and in our case mainly onto the WIG modes as the basis functions are
 454 derived for the state of rest. When the linear modal decomposition will be replaced by
 455 the non-linear decomposition (Ko et al., 1981), the planetary-scale divergence, now in
 456 IG modes, should become a part of the balanced flow providing an easier interpretation
 457 of the remaining IG modes as unbalanced flow.

458 The Rossby wave E_D^k is 2-3 orders of magnitude smaller than the IG E_D^k at the same
 459 levels and scales. The Rossby E_D^k peaks across the stratopause at $k = 2$ in midlatitudes
 460 (Fig. 6h) and at $k = 1$ in high latitudes of the winter hemisphere (SH) (Fig. 7h). Even
 461 though the peak extends well above 1 hPa, it is possibly affected by the artificial sponge
 462 layer in ERA5. There is a strong vertical gradient in the Rossby E_D^k amplitudes in the
 463 upper stratosphere (Fig. 6h and Fig. 7h), associated with the Rossby wave attenuation
 464 as they propagate upward in the winter stratosphere (e.g., Charney & Drazin, 1961). In

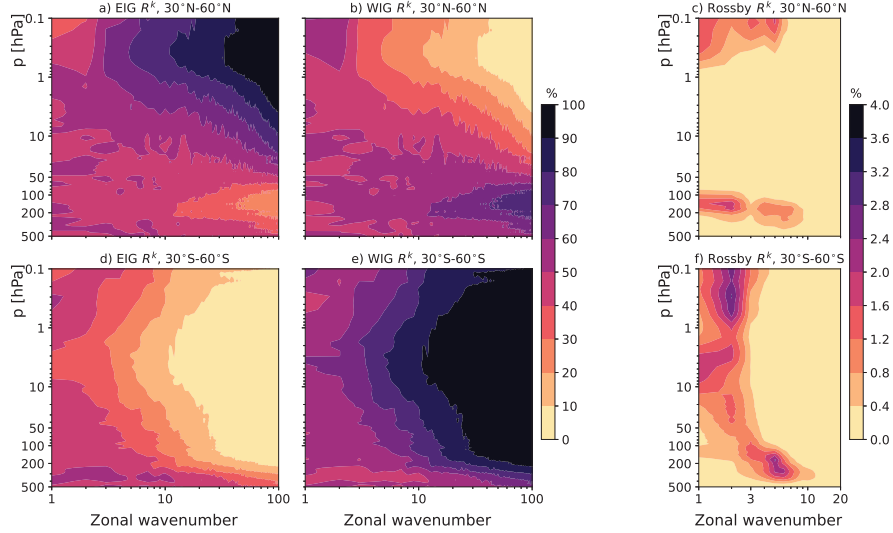


Figure 8. Relative contribution to E_D^k by the (a,d) EIG, (b,e) WIG and (c,f) Rossby modes in the latitude belt (a-c) 30°N – 60°N and (d-f) 30°S – 60°S .

465 the troposphere, a secondary maximum in the Rossby E_D^k at synoptic scales in midlat-
 466 itudes can be seen near 300 hPa, with a stronger peak in the winter hemisphere. An
 467 increased signal at the same levels and scales is present also in the non-Rossby E_D^k
 468 spectra (Fig. 6e) that can be coupled with ageostrophic circulation and inertia-gravity waves
 469 excited by jets and baroclinic processes (e.g., O’Sullivan & Dunkerton, 1995; Plougonven
 470 & Zhang, 2014).

471 How large is the contribution of the IG modes to divergent power at different lev-
 472 els and scales? This can be quantified by evaluating Eq. (14) and the result is presented
 473 in Fig. 8 for the two midlatitude belts. It shows that the stratospheric mesoscale diver-
 474 gence power in the winter hemisphere is up to 90% due to WIG modes because of the
 475 filtering effect of the background flow (Fig. 8d-e). A small part is due to the planetary
 476 Rossby waves, 3-4% at most at $k = 5-10$ in the upper troposphere and at $k = 1, 2$
 477 in the upper stratosphere (Fig. 8f). Similarly, due to middle atmosphere easterlies in the
 478 summer hemisphere (NH), the mesoscale E_D^k above 10 hPa is up to 90% EIG (Fig. 8a).
 479 Lower down in the upper troposphere and across the tropopause layer, EIG and WIG
 480 modes contribute about equally to divergence power reflecting no direction preference
 481 for mesoscale gravity waves and divergence sources in the troposphere. The higher lat-
 482 itudes (not shown) have % very similar to midlatitudes but with the maximal contribu-
 483 tion of Rossby modes at $k = 1$ near 1 hPa and making less than 1% of total E_D^k (not
 484 shown).

485 3.2 Tropics and Subtropics

486 The tropical divergence power spectra are presented in Fig. 9. While overall sim-
 487 ilar to extratropical spectra, maxima in tropical non-Rossby E_D^k spectra extends from
 488 synoptic to planetary scales in the upper troposphere (Fig. 9a vs. Fig. 6a). This is a sig-
 489 nature of the large-scale non-Rossby waves including the Kelvin and MRG waves in the
 490 upper tropical atmosphere (e.g., Wheeler et al., 2000; Yang et al., 2003; Žagar et al., 2009a;
 491 Kiladis et al., 2009, 2016), known to drive middle atmosphere processes such as the QBO.

492 Divergence defines the vertical velocity which in turn defines the vertical momentum fluxes
 493 (e.g., Baldwin et al., 2001; Lu et al., 2020).

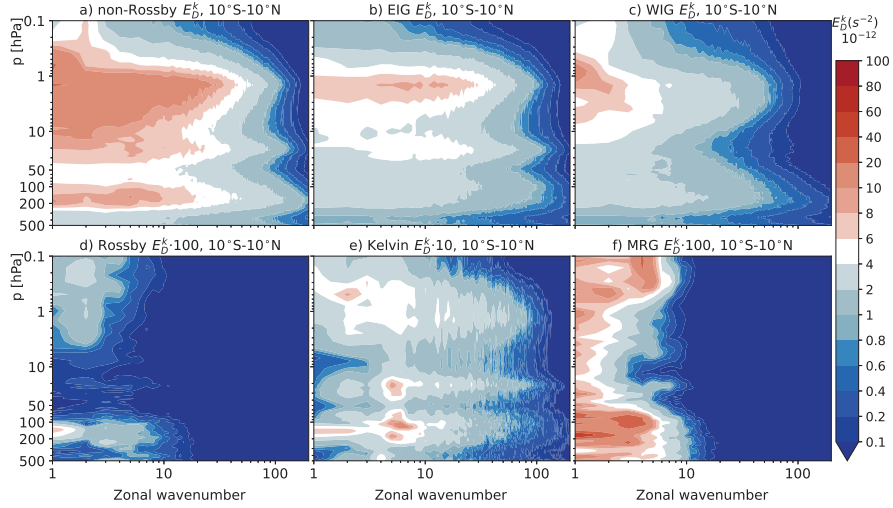


Figure 9. Level-by-level (a) non-Rossby, (b) EIG, (c) WIG, (d) Rossby, (e) Kelvin and (f) MRG mode divergence power spectra E_D^k averaged within 10°N – 10°S . The Rossby and MRG spectra are multiplied by 100, and the Kelvin wave spectrum is multiplied by 10. Note the non-linear contour intervals.

494 The decomposition of the non-Rossby divergence into the four wave types provides
 495 scale- and altitude-dependent differences between the Kelvin and MRG waves and the
 496 IG modes. The vertical distributions of E_D^k are expected to be strongly coupled with the
 497 shear lines of the zonal-mean zonal flow that is therefore included in Fig. 10 which shows
 498 relative power in the five wave species. Transitions between easterlies and westerlies ex-
 499 plain differences between the EIG and WIG E_D^k and their relative contributions to the
 500 total divergence power spectrum. It shows that the EIG exceeds the WIG E_D^k at sub-
 501 synoptic scales in the stratosphere (Fig. 9b vs. Fig. 9c and Fig. 10a vs. Fig. 10b), es-
 502 pecially in the layer with westerly shear around 30 hPa. Both EIG and WIG signals max-
 503 imize near 1 hPa (Fig. 9b,c), most likely due to the sponge layer, but at different scales:
 504 the WIG E_D^k has the largest amplitude at $k = 1-3$ whereas a broad maximum of EIG
 505 E_D^k is centered around $k = 10$ that corresponds to wavelength of about 2000 km. In
 506 the upper troposphere without strong shear lines in the mean zonal flow, EIG and WIG
 507 modes have more similar contributions to E_D^k . The Rossby mode divergence power in
 508 August 2018 was at least two orders of magnitudes smaller than non-Rossby E_D^k every-
 509 where except at $k = 1$ near 150 hPa (Fig. 9d). The Rossby E_D^k makes no more than
 510 1.2% of E_D^k at $k = 1$ between 100-200 hPa (Fig. 10c), whereas nearly everywhere else
 511 in wave space it is below 0.5%.

512 There is a large difference between the IG and the Kelvin and MRG mode diver-
 513 gence in both amplitudes and scale selection of the signals (Fig. 9e,f). First of all, the
 514 Kelvin wave divergence power in August 2018 was an order of magnitude greater than
 515 the MRG E_D^k . The Kelvin wave signal peaks at several synoptic-scale wavenumbers in
 516 the upper troposphere and there is a secondary peak at $k = 1$ within the tropopause
 517 layer (Fig. 9e). At these wavenumbers, the Kelvin E_D^k makes up to about 25% of the to-
 518 tal divergence power (Fig. 10d). For the MRG waves, the E_D^k spectra are more flat at
 519 large scales with little signal beyond $k = 10$ in the UTLS region (Fig. 9f). The MRG

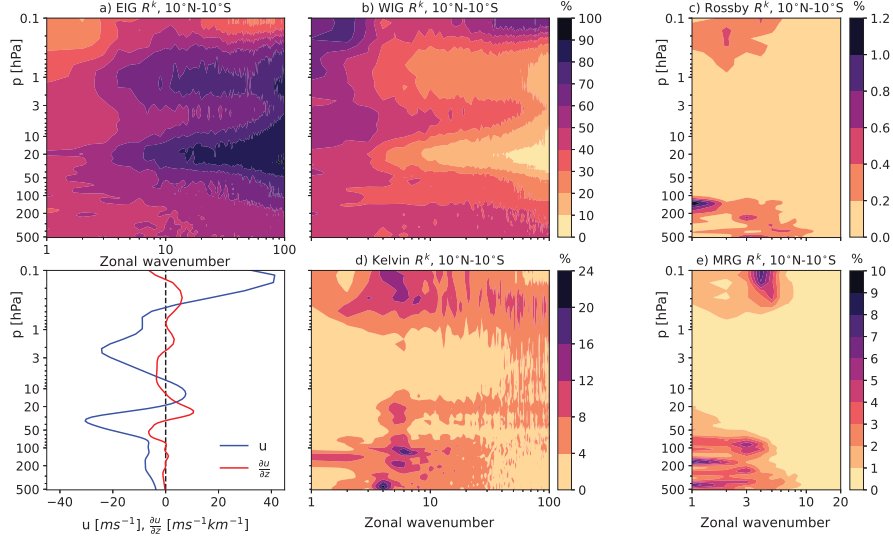


Figure 10. Relative contribution to E_D^k by (a) EIG, (b) WIG, (c) Rossby, (d) Kelvin and (e) MRG modes in the tropical belt 10°N – 10°S . The additional panel shows the profile of the zonal mean zonal wind u and its shear as $\partial u/\partial z$.

520 contribution to the total E_D^k at individual wavenumbers in August 2018 does not exceed
 521 10% which is twice smaller than for the Kelvin waves.

522 The five E_D^k spectra are additionally shown in Fig. 11 for two tropical layers to com-
 523 pare the spectral slopes of E_D^k for various wave species with respect to their frequencies
 524 discussed in Section 2. The two layers are the 100–200 hPa layer with the maximal diver-
 525 gence in the upper troposphere and the 20–30 hPa layer with the maximal westerly
 526 shear in the stratosphere. Figure 11a shows dominance of EIG over WIG E_D^k in the layer
 527 where the WIG waves likely meet the critical levels. The EIG E_D^k spectra are nearly white
 528 or have a slightly positive slope over a range of $k \approx 5 - 50$. The WIG and EIG E_D^k
 529 spectra are more similar within the tropopause layer (Fig. 11b) and have a more com-
 530 parable power at most scales.

531 The shape of the Kelvin E_D^k spectra is similar to the WIG and EIG spectra as could
 532 be expected based on the same frequency–zonal wavenumber, $\nu - k$, scaling. But, the
 533 Kelvin E_D^k amplitude is 1–2 orders of magnitude smaller power compared to EIG modes.
 534 The power in both IG and Kelvin waves drops sharply beyond $k \approx 100$ which is most
 535 likely due to the insufficient ERA5 model resolution. The MRG and Rossby E_D^k spec-
 536 tra are very steep beyond planetary and large synoptic scales which is expected given
 537 their $\nu - k$ scaling. The MRG waves in August 2018 had a comparable signal to the Kelvin
 538 E_D^k only at planetary scales and more so in the tropopause layer.

539 Why there is relatively little divergence in the Kelvin and MRG waves compared
 540 to IG modes? The answer lies in their particular nature of being a scale-dependent mix-
 541 ture of divergent and rotational flow. The Hough decomposition followed by the Helmholtz
 542 decomposition can quantify the divergent and rotational portions of the Kelvin and MRG
 543 kinetic energies as a function of the zonal wavenumber (Eq. 13). Its application to our
 544 August 2018 data is shown in Fig. 12. At $k = 1$, the Kelvin wave is predominantly rota-
 545 tional (Fig. 12a), similar to its climatological spectrum (Žagar et al., 2022). The di-
 546 vergent energy becomes dominant for $k > 2$ and makes most of the kinetic energy at
 547 subsynoptic scales. The total and divergent Kelvin wave kinetic energy spectrum is some-

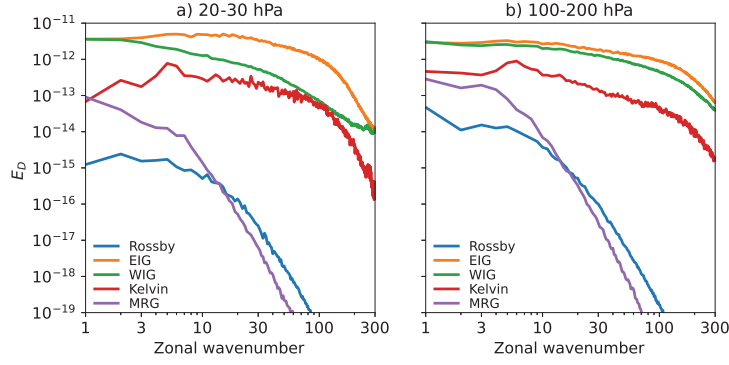


Figure 11. Divergence power spectra E_D^k averaged for latitudes 10°N – 10°S and a) 20–30 hPa, b) 100–200 hPa layers. E_D^k is evaluated separately for the Rossby (R), EIG, WIG, Kelvin (K), and MRG waves.

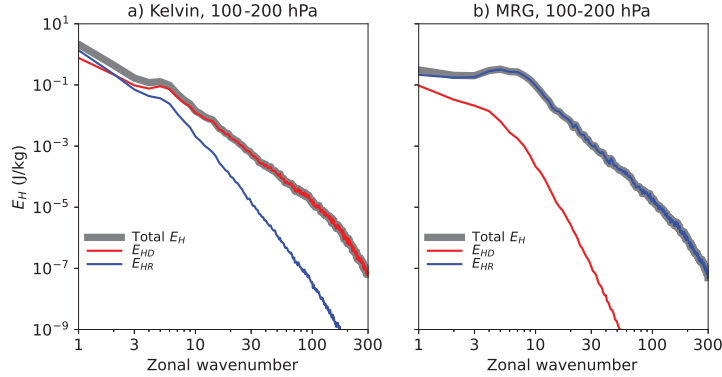


Figure 12. The horizontal kinetic energy spectra of the a) Kelvin and b) MRG waves averaged for levels between 100 and 200 hPa for August 2018 ERA5 data. The total kinetic energy E_H is split between the divergent, E_{HD} , and rotational, E_{HR} , parts. See the text for details.

548 what shallower than a k^{-3} power law. The MRG waves within the 100–200 hPa layer are
 549 characterised by negligible divergent kinetic energy beyond planetary scales. The total
 550 and rotational kinetic energy spectra of the MRG waves follow a k^{-3} power law similar
 551 to the Rossby waves (not shown). This explains an almost negligible MRG E_D^k signal
 552 in Fig. 9 outside large scales.

553 Finally, we show in Fig. 13 the E_D^k spectra for the subtropical belts of both hemi-
 554 spheres that complement the physical picture discussed for other latitudes. The largest
 555 difference compared to other regions is between EIG and Rossby modes for the NH and
 556 SH subtropics. The EIG E_D^k is stronger in NH than in SH, especially at subsynoptic scales
 557 in the upper stratosphere (Fig. 13b vs. Fig. 13e). This may be associated with stronger
 558 gravity wave activity in the monsoon latitudes. Compared to midlatitude spectra (Fig. 6),
 559 the IG E_D^k in the upper troposphere is more significant at planetary scales, like in the
 560 tropics. This is to a small extent also related to the Kelvin and MRG signals extending
 561 beyond 10° away from the equator (Fig. 13h,i,k,l). The meridional half-scale of both waves
 562 is known to be 5° – 10° in the troposphere but grows significantly greater in the upper tro-
 563 posphere (e.g., Knippertz et al., 2022; Yang et al., 2023) and mesosphere (e.g., Garcia

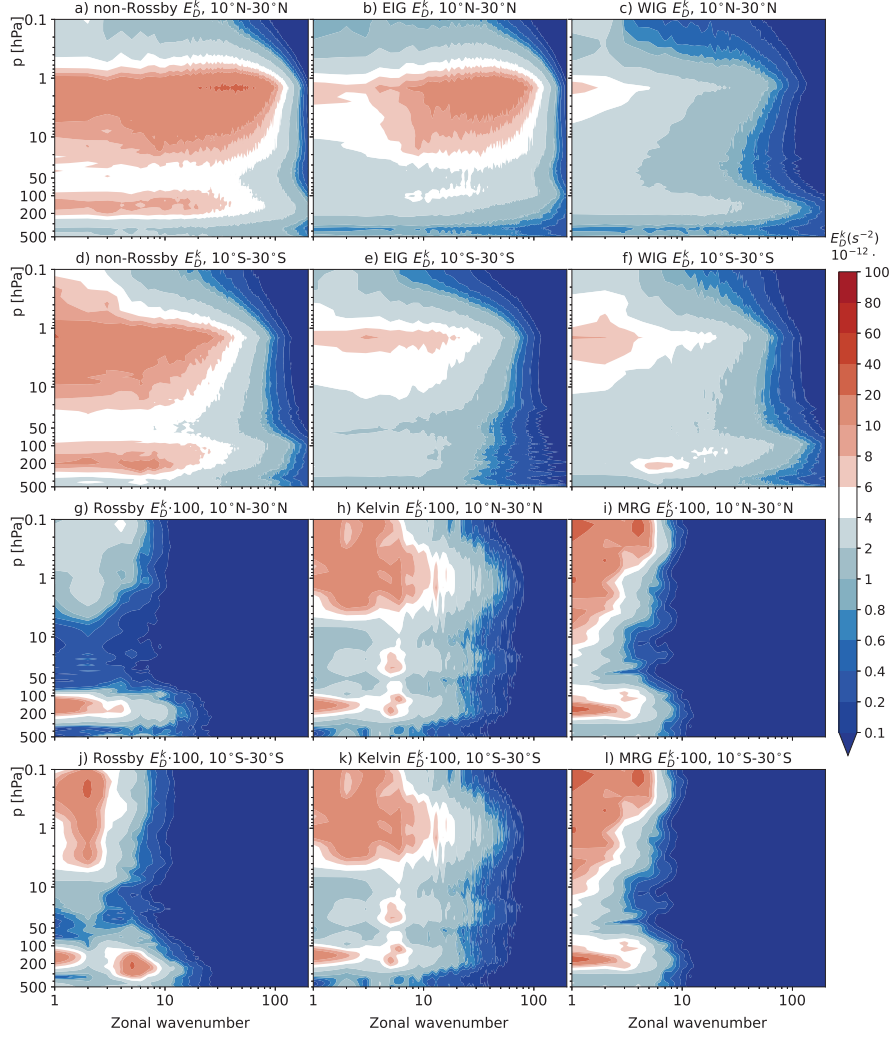


Figure 13. As in Fig. 9 but for the latitude belt (a-c and g-i) $10^{\circ}\text{N}-30^{\circ}\text{N}$ and (d-f and j-l) $10^{\circ}\text{S}-30^{\circ}\text{S}$. The Rossby, Kelvin, and MRG divergence spectra are multiplied by 100. Note the nonlinear contour intervals.

564 et al., 2005). The Kelvin wave and MRG wave meridional scales in the real-time ECMWF
 565 analyses and forecasts can be seen at [https://modes.cen.uni-hamburg.de/products#](https://modes.cen.uni-hamburg.de/products#KW)
 566 KW and <https://modes.cen.uni-hamburg.de/products#MRG>, respectively. It can be noticed
 567 in Fig. 13 that the Kelvin E_D^k is relatively smaller than the MRG E_D^k compared
 568 to the $10^{\circ}\text{S}-10^{\circ}\text{N}$ belt which is because the Kelvin wave divergence is centered at the equator
 569 whereas the MRG wave divergence is largest away from the equator (see Fig. 1). At
 570 subsynoptic scales in the summer (NH) subtropical stratosphere, the EIG E_D^k makes over
 571 80% of the total divergent power. It is the opposite in the upper troposphere and tropopause
 572 layers, where the WIG modes contain the majority of divergence power in subtropical
 573 SH (not shown). Both properties are easily associated with the season and the background
 574 flow. Finally, the Rossby mode divergence power in August 2018 has its global maximum
 575 between 300 and 200 hPa levels in SH subtropics (not shown).

4 Discussion and Conclusions

This paper extended the application of the linear normal-mode decomposition to divergence, as a key intermediate step towards a unified decomposition of the vertical velocity (Žagar et al., 2023) and the vertical momentum fluxes that remain an order one challenge for weather and climate models (e.g., Geller et al., 2013), even for km-scale models (e.g., Polichtchouk et al., 2022). An important novel aspect of our approach is the co-existence of the tropical Rossby, IG, Kelvin and MRG waves at the same zonal scales and implicitly also at the same frequencies.

It has long been established that subsynoptic scales of motions largely project onto IG modes (e.g., Tanaka & Žagar, 2020, and references therein). Žagar et al. (2009b, 2009a) demonstrated that filtering IG modes back to physical space produces physically informative horizontal winds, geopotential height and temperature perturbations associated with Rossby and IG waves, and equatorial waves in particular. Scale-selective filtering of IG modes shows that divergence-dominated flows span the scales from the mean-zonal state (i.e. Hadley cell) (Puri, 1983; Pikovnik et al., 2022) to large-scale waves (Puri, 1988; Žagar et al., 2009a) and smaller-scale coherent structures. The latter are more difficult to identify as waves within the tropical troposphere because of their coupling with convection, with the nonlinear coupling represented by smaller equivalent depths (i.e. wave speeds) compared to the values for the dry waves (e.g., Kiladis et al., 2009; Knippertz et al., 2022). The 3D normal-mode decomposition couples the vertical structure of waves and their horizontal properties through the equivalent depths. Multiple depths or VSFs are involved in the representation of wave signals within various layers and not every small-scale structure projecting on IG modes is a wave in the sense that its phase speed and energy propagation can be diagnosed for example by the hodograph method (Hamilton, 1991; Sato & Yamada, 1994; Fritts & Alexander, 2003). On the other hand, this is easily demonstrated for large-scale waves such as the Kelvin wave (Žagar et al., 2009a), and for extratropical stratospheric gravity waves (Dörnbrack et al., 2018). Furthermore, Žagar et al. (2017) demonstrated by the hodograph method that also tropospheric extratropical gravity waves can be filtered out using the NMF decomposition.

In this paper, we focused on scales from hundreds of km to synoptic and planetary wavenumbers which are commonly identified as most relevant for equatorial waves. Presented divergence power spectra reflect physical properties of the flow, some of which have been well established, primarily in the extratropics. In particular, even though we perform the wavenumber decomposition that does not explicitly account for wave propagation, i.e. for their frequencies and the effects of the vertical variations of the large-scale background wind through which the waves propagate, the spectral distribution of IG divergence in extratropics and throughout the middle atmosphere is easily explained by considering effects of the background wind.

The key new result of this study concerns the decomposition of divergence and divergence power in the tropics. This is enabled by a new method that provides divergence as a function of the pressure level and latitude. In order to quantify the divergence power in various wave species, we compare in Fig. 14 portions of the zonally-integrated divergence power of different waves within seven latitude belts. To make the discussion of vertically-varying E_D^k easier, the zonal-mean zonal wind profile and its vertical shear are added.

Focusing first on the tropical distributions (red lines in panels a) to e) of Fig. 14), we can see that the Kelvin waves make 4-6% of the total divergent power in the tropical troposphere with a maximum around 150 hPa, where the Kelvin wave signal is strongest (Žagar et al., 2022). The tropical MRG wave portion of E_D^k in the troposphere is up to 0.5% or an order of magnitude smaller than for the Kelvin waves. An approximate estimate of divergence portions is given by the square roots of power implying about 20% and about 7% of divergence associated with the Kelvin and MRG waves in tropical belt 10°S-10°N (as square roots of 0.05 and 0.005 for the Kelvin and MRG waves, respectively).

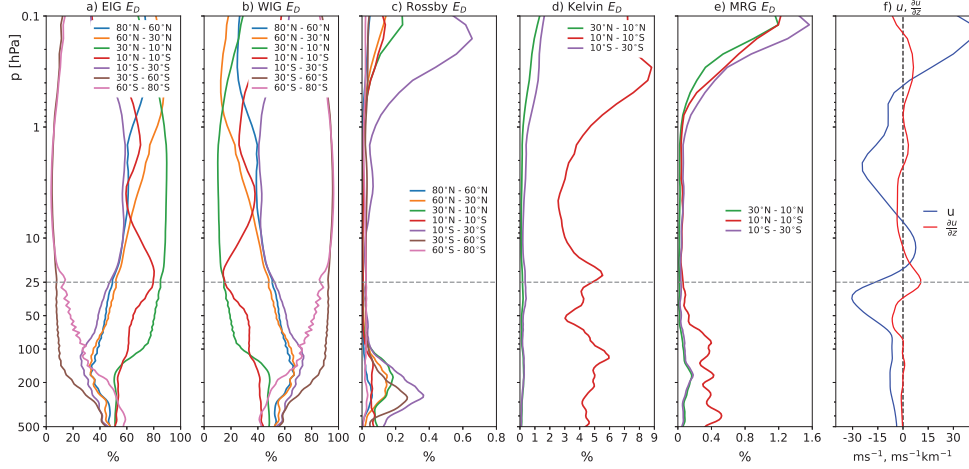


Figure 14. Vertical profiles of the relative contributions of the a) EIG, b) WIG, c) Rossby, d) Kelvin, and e) MRG divergence power zonally integrated for $k = 1 - 100$ within different latitude belts. f) Vertical profile of the zonal-mean zonal wind and its vertical shear in the tropical belt $10^{\circ}\text{S}-10^{\circ}\text{N}$. Dashed line represents the level of the maximal shear.

628 These percentages can grow much larger in some wave numbers. In August 2018, the Kelvin
 629 wave power was up to 24% at several synoptic scales implying almost 50% of the hor-
 630 izontal wind divergence due to the Kelvin waves at these scales. Similarly, 10% of the
 631 divergent power due to MRG waves at planetary scales in the tropopause in August 2018
 632 implies about 1/3 of the horizontal wind divergence at these wavenumbers. Together,
 633 the two waves made up to 6% of the zonally-integrated divergence power (E_D) in Au-
 634 gust 2018 which is about 25% of divergence. At selected wavenumber, these percentages
 635 grow much larger calling for studies of longer datasets in reanalyses and climate mod-
 636 els and of temporal variance of E_D . While longer datasets are yet to be analysed, our
 637 results advise against using divergence as a proxy for the Kelvin waves. The results also
 638 support small amplitudes of the MRG waves reported by Lu et al. (2020) as realistic to
 639 the extent of the realism of reanalysis data. The relatively small roles of the Kelvin and
 640 MRG waves in tropical divergence are explained by comparing their rotational and di-
 641 vergent kinetic energy spectra. The MRG waves at all scales and $k = 1$ Kelvin wave
 642 are predominantly rotational in the upper tropical troposphere. Although divergence above
 643 1 hPa in ERA5 is not trustworthy, we note a growing portion of the MRG and Kelvin
 644 wave divergence power above 1 hPa (Fig. 14d,e), with the MRG maximum just above
 645 the peak westerly flows near 0.2 hPa.

646 The majority of non-Rossby divergence is approximately equally distributed be-
 647 tween the EIG and WIG modes in the tropical troposphere whereas the stratospheric
 648 partitioning depends on the background flow and its shear (Fig. 14a,b). In the extrat-
 649 ropics, over 90% divergence power above 150 hPa in the winter hemisphere (SH in Au-
 650 gust 2018) is associated with WIG modes, and the same applies to EIG modes in the
 651 summer hemisphere (NH). Finally, the Rossby wave divergence power is below 0.4% im-
 652 plying up to 6% of global divergence due to the beta effect (the geostrophic wind diver-
 653 gence on the sphere, $-v_g f / \beta$). The E_D of 0.3-0.4% peaks near 300 hPa in winter asso-
 654 ciated with synoptic-scale baroclinic waves and jets that are known to be stronger in the
 655 winter hemisphere. In summer hemisphere extratropics, the Rossby wave divergence peak
 656 makes about 0.2% of E_D near 200 hPa (Fig. 14c).

Data Availability Statement

The ERA5 data were obtained from Copernicus Climate Change Service (C3S, 2017), downloaded in March 2021. Hough expansion coefficients of ERA5 input fields and Fourier coefficients of divergence associated with different wave types can be found publicly available at <https://doi.org/10.5281/zenodo.10080436> (Neduhal, 2023). The default version of the MODES software is available via <http://modes.cen.uni-hamburg.de>. Figures were made with Matplotlib version 3.2.1 (Hunter, 2007), available under the Matplotlib license at <https://matplotlib.org/>.

Acknowledgments

This paper is a contribution to the Collaborative Research Centre TRR 181 “Energy Transfers in Atmosphere and Ocean” funded by the Deutsche Forschungsgemeinschaft (DFG, German Research Foundation), project no. 274762653. Ž. Zaplotnik was supported by the Slovenian Research Agency (ARRS), grant no. J1-9431 and Program P1-0188. We thank Sergiy Vasylykevych and Richard Blender for the discussions.

References

- Adams, J. C., & Swarztrauber, P. N. (2001). SPHEREPACK 3.0: A model development facility. *Mon. Wea. Rev.*, *127*, 1872–1878. doi: <https://doi.org/10.1080/16000870.2016.1271563>
- Baldwin, M. P., Gray, L. J., Dunkerton, T. J., Hamilton, K., Haynes, P. H., Randel, W. J., . . . M, T. (2001). The quasi-biennial oscillation. *Rev. Geophys.*, *39*(2), 179–229. doi: <https://doi.org/10.1080/16000870.2016.1271563>
- Banacos, P. C., & Schultz, D. M. (2005). The use of moisture flux convergence in forecasting convective initiation: Historical and operational perspectives. *Weather and Forecasting*, *20*(3), 351–366. doi: <https://doi.org/10.1175/WAF858.1>
- Berry, G., & Reeder, M. J. (2014). Objective identification of the intertropical convergence zone: Climatology and trends from the era-interim. *J. Clim.*, *27*(5), 1894–1909. doi: <https://doi.org/10.1175/JCLI-D-13-00339.1>
- Bley, S., Rennie, M., Žagar, N., Pinol Sole, M., Straume, A. G., Antifaev, J., . . . others (2022). Validation of the aeolus l2b rayleigh winds and ecmwf short-range forecasts in the upper troposphere and lower stratosphere using loon super pressure balloon observations. *Q. J. R. Meteorol. Soc.*, *148*(749), 3852–3868. doi: <https://doi.org/10.1002/qj.4391>
- Bony, S., & Stevens, B. (2019). Measuring area-averaged vertical motions with dropsondes. *J. Atmos. Sci.*, *76*(3), 767–783. doi: <https://doi.org/10.1175/JAS-D-18-0141.1>
- Bony, S., Stevens, B., Ament, F., Bigorre, S., Chazette, P., Crewell, S., . . . others (2017). Eurec4a: A field campaign to elucidate the couplings between clouds, convection and circulation. *Surv. Geophys.*, *38*, 1529–1568. doi: <https://doi.org/10.1007/s10712-017-9428-0>
- Burgess, B. H., Erler, A. R., & Shepherd, T. G. (2013). The troposphere-to-stratosphere transition in kinetic energy spectra and nonlinear spectral fluxes as seen in ECMWF analyses. *J. Atmos. Sci.*, *70*(2), 669–687. doi: <https://doi.org/10.1175/JAS-D-12-0129.1>
- C3S. (2017). *ERA5: Fifth generation of ECMWF atmospheric reanalyses of the global climate. Accessed on Mar-2021.* [dataset]. Retrieved from <https://cds.climate.copernicus.eu/#/home>
- Charney, J. G., & Drazin, P. G. (1961). Propagation of planetary scale disturbances from the lower into the upper atmosphere. *J. Geophys. Res.*, *66*, 83–109. doi: <https://doi.org/10.1029/JZ066i001p00083>
- Dai, A., & Deser, C. (1999). Diurnal and semidiurnal variations in global surface

- 708 wind and divergence fields. *J. Geophys. Res.*, *104*(D24), 30853–31809. doi:
709 <https://doi.org/10.1029/1999JD900927>
- 710 Dörnbrack, A., Bechtold, P., & Schumann, U. (2022). High-resolution aircraft ob-
711 servations of turbulence and waves in the free atmosphere and comparison with
712 global model predictions. *J. Geophys. Res. Atmos.*, *127*(16), e2022JD036654.
713 doi: <https://doi.org/10.1029/2022JD036654>
- 714 Dörnbrack, A., Gisinger, S., Kaifler, N., Portele, T., Bramberger, M., Rapp,
715 M., ... Jelić, D. (2018). Gravity waves excited during a minor sudden
716 stratospheric warming. *Atmos. Chem. Phys.*, *18*(17), 12915–12931. doi:
717 <https://doi.org/10.5194/acp-18-12915-2018>
- 718 Ern, M., & Preusse, P. (2009). Wave fluxes of equatorial Kelvin waves and QBO
719 zonal wind forcing derived from SABER and ECMWF temperature space-time
720 spectra. *Atmos. Chem. Phys.*, *9*, 3957–3986. doi: [https://doi.org/10.5194/
721 acp-9-3957-2009](https://doi.org/10.5194/acp-9-3957-2009)
- 722 Fritts, D. C., & Alexander, J. M. (2003). Gravity wave dynamics and effects in
723 the middle atmosphere. *Rev. Geophys.*, *41*(1). doi: [https://doi.org/10.1029/
724 2001RG000106](https://doi.org/10.1029/2001RG000106)
- 725 Garcia, R. R., Lieberman, R., Russell, J. M., & Mlynczak, M. G. (2005). Large-scale
726 waves in the mesosphere and lower thermosphere observed by SABER. *J. At-
727 mos. Sci.*, *62*(12), 4384–4399. doi: <https://doi.org/10.1175/JAS3612.1>
- 728 Geller, M. A., Alexander, M. J., Love, P. T., Bacmeister, J., Ern, M., Hertzog, A.,
729 ... Zhou, T. (2013). A comparison between gravity wave momentum fluxes
730 in observations and climate models. *J. Climate*, *26*(17), 6383–6405. doi:
731 <https://doi.org/10.1175/JCLI-D-12-00545.1>
- 732 Gill, A. E. (1980). Some simple solution for heat-induced tropical circulation.
733 *Q. J. R. Meteorol. Soc.*, *106*(449), 447–462. doi: [https://doi.org/10.1002/
734 qj.49710644905](https://doi.org/10.1002/qj.49710644905)
- 735 Gisinger, S., Polichtchouk, I., Dörnbrack, A., Reichert, R., Kaifler, B., Kaifler, N.,
736 ... Sandu, I. (2022). Gravity-wave-driven seasonal variability of temperature
737 differences between ecmwf ifs and rayleigh lidar measurements in the lee of
738 the southern andes. *J. Geophys. Res. Atmos.*, *127*(13), e2021JD036270. doi:
739 <https://doi.org/10.1029/2021JD036270>
- 740 Gupta, A., Birner, T., Dörnbrack, A., & Polichtchouk, I. (2021). Importance
741 of gravity wave forcing for springtime southern polar vortex breakdown
742 as revealed by era5. *Geophys. Res. Lett.*, *48*(10), e2021GL092762. doi:
743 <https://doi.org/10.1029/2021GL092762>
- 744 Hamilton, K. (1991). Climatological statistics of stratospheric inertia-gravity waves
745 deduced from historical rocketsonde wind and temperature data. *J. Geophys.
746 Res.*, *96*(20), 831–20. doi: <https://doi.org/10.1029/91JD02188>
- 747 Hersbach, H., Bell, B., Berrisford, P., Hirahara, S., Horányi, A., Muñoz-Sabater, J.,
748 ... Thépaut, J.-N. (2020). The era5 global reanalysis. *Q. J. R. Meteorol. Soc.*,
749 *146*(730), 1999–2049. doi: <https://doi.org/10.1002/qj.3803>
- 750 Holton, J. R. (2004). *An introduction to dynamic meteorology* (4th ed.; R. Dmowska
751 & J. R. Holton, Eds.). Burlington, MA: Elsevier Academic Press.,
- 752 Hunter, J. D. (2007). Matplotlib: A 2d graphics environment. *Computing in Science
753 & Engineering*, *9*(3), 90–95. doi: <https://doi.org/10.1109/MCSE.2007.55>
- 754 Jakobsen, F., & Madsen, H. (2004). Comparison and further development of para-
755 metric tropical cyclone models for storm surge modelling. *J. Wind. Eng. Ind.
756 Aerodyn.*, *92*(5), 375–391. doi: <https://doi.org/10.1016/j.jweia.2004.01.003>
- 757 Kasahara, A. (2020). 3d normal mode functions (nmfs) of a global baroclinic at-
758 mospheric model. In N. Žagar & J. Tribbia (Eds.), *Modal view of atmospheric
759 variability: Applications of normal-mode function decomposition in weather
760 and climate research* (pp. 1–61). Cham: Springer International Publishing. doi:
761 https://doi.org/10.1007/978-3-030-60963-4_1
- 762 Kiladis, G. N., Dias, J., & Gehne, M. (2016). The Relationship between Equatorial

- 763 Mixed Rossby–Gravity and Eastward Inertio-Gravity Waves. Part I. *J. Atmos.*
 764 *Sci.*, 73(5), 2123–2145. doi: <https://doi.org/10.1175/JAS-D-15-0230.1>
- 765 Kiladis, G. N., Wheeler, M. C., Haertel, P. T., Straub, K. H., & Roundy, P. E.
 766 (2009). Convectively coupled equatorial waves. *Rev. Geophys.*, 47(2). doi:
 767 <https://doi.org/10.1029/2008RG000266>
- 768 Kim, Y.-H., & Chun, H.-Y. (2015). Contributions of equatorial wave modes and pa-
 769 rameterized gravity waves to the tropical QBO in HadGEM2. *J. Geophys. Res.*
 770 *Atmos.*, 120(3), 1065–1090. doi: <https://doi.org/10.1002/2014JD022174>
- 771 Kimberlain, T. B. (2016). *Tropical storm Fiona*. National Hurricane Center. Re-
 772 trieved from https://www.nhc.noaa.gov/data/tcr/AL062016_Fiona.pdf
- 773 Knippertz, P., Gehne, M., Kiladis, G. N., Kikuchi, K., Rasheeda Satheesh, A.,
 774 Roundy, P. E., . . . Wheeler, M. C. (2022). The intricacies of identify-
 775 ing equatorial waves. *Q. J. R. Meteorol. Soc.*, 148(747), 2814–2852. doi:
 776 <https://doi.org/10.1002/qj.4338>
- 777 Ko, S. D., Tribbia, J. J., & Boyd, J. P. (1981). Energetics analysis of a mul-
 778 tilevel global spectral model. Part I: Balanced energy and transient en-
 779 ergy. *Mon. Wea. Rev.*, 117(9), 1941–1953. doi: [https://doi.org/10.1175/](https://doi.org/10.1175/1520-0493(1989)117<1941:EAOAMG>2.0.CO;2)
 780 [1520-0493\(1989\)117<1941:EAOAMG>2.0.CO;2](https://doi.org/10.1175/1520-0493(1989)117<1941:EAOAMG>2.0.CO;2)
- 781 Lambert, S. J. (1984). A global available potential energy-kinetic energy budget
 782 in terms of the two-dimensional wavenumber for the FGGE year. *Atmos. -*
 783 *Ocean.*, 22(3), 265–282. doi: <https://doi.org/10.1080/07055900.1984.9649199>
- 784 Lott, F., & Miller, M. J. (1997). A new subgrid-scale orographic drag parametriza-
 785 tion: Its formulation and testing. *Q. J. R. Meteorol. Soc.*, 123(537), 101–127.
 786 doi: <https://doi.org/10.1002/qj.49712353704>
- 787 Lu, Y., Wu, T., Jie, W., Scaife, A. A., Andrews, M. B., & Richter, J. H. (2020).
 788 Variability of the Stratospheric Quasi-Biennial Oscillation and Its Wave For-
 789 cing Simulated in the Beijing Climate Center Atmospheric General Circula-
 790 tion Model. *J. Atmos. Sci.*, 77(1), 149–165. doi: [https://doi.org/10.1175/](https://doi.org/10.1175/JAS-D-19-0123.1)
 791 [JAS-D-19-0123.1](https://doi.org/10.1175/JAS-D-19-0123.1)
- 792 Matsuno, T. (1966). Quasi-geostrophic motions in the equatorial area. *J. Meteor.*
 793 *Soc. Japan*, 44(1), 25–42. doi: <https://doi.org/10.2151/jmsj1965.44.1.25>
- 794 Nappo, C. J. (2002). *An introduction to atmospheric gravity waves* (2nd ed.). Ams-
 795 terdam: Academic Press, Elsevier Science.
- 796 Neduhal, V. (2023). *Decomposition of the horizontal wind divergence using modes*
 797 [dataset]. Zenodo. doi: <https://doi.org/10.5281/zenodo.10080436>
- 798 Orr, A., Bechtold, P., Scinocca, J., Ern, M., & Janiskova, M. (2010). Improved
 799 middle atmosphere climate and forecasts in the ECMWF model through a
 800 non-orographic gravity wave drag parametrization. *J. Climate*, 23(22), 5905–
 801 5926. doi: <https://doi.org/10.1175/2010JCLI3490.1>
- 802 O’Sullivan, D., & Dunkerton, T. J. (1995). Generation of inertia–gravity waves in a
 803 simulated life cycle of baroclinic instability. *J. Atmos. Sci.*, 52(21), 3695–3716.
 804 doi: [https://doi.org/10.1175/1520-0469\(1995\)052<3695:GOIWIA>2.0.CO;2](https://doi.org/10.1175/1520-0469(1995)052<3695:GOIWIA>2.0.CO;2)
- 805 Pikovnik, M., Zaplotnik, v., Boljka, L., & Žagar, N. (2022). Metrics of the hadley
 806 circulation strength and associated circulation trends. *Weather Clim. Dynam.*,
 807 3(2), 625–644. doi: <https://doi.org/10.5194/wcd-3-625-2022>
- 808 Plougonven, R., & Zhang, F. (2014). Internal gravity waves from atmospheric
 809 jets and fronts. *Rev. Geophys.*, 52(1), 33–76. doi: [https://doi.org/10.1002/](https://doi.org/10.1002/2012RG000419)
 810 [2012RG000419](https://doi.org/10.1002/2012RG000419)
- 811 Polichtchouk, I., Van Niekerk, A., & Wedi, N. (2023). Resolved Gravity Waves
 812 in the Extratropical Stratosphere: Effect of Horizontal Resolution In-
 813 crease from O (10) to O (1) km. *J. Atmos. Sci.*, 80(2), 473–486. doi:
 814 <https://doi.org/10.1175/JAS-D-22-0138.1>
- 815 Polichtchouk, I., Wedi, N., & Kim, Y.-H. (2022). Resolved gravity waves in
 816 the tropical stratosphere: Impact of horizontal resolution and deep con-
 817 vection parametrization. *Q. J. R. Meteorol. Soc.*, 148(742), 233–251. doi:

- 818 <https://doi.org/10.1002/qj.4202>
- 819 Puri, K. (1983). The relationship between convective adjustment Hadley circulation
820 and normal modes of the ANMRC spectral model. *Mon. Wea. Rev.*, *111*(1),
821 23–33. doi: [https://doi.org/10.1175/1520-0493\(1983\)111<0023:TRBCAH>2.0](https://doi.org/10.1175/1520-0493(1983)111<0023:TRBCAH>2.0.CO;2)
822 .CO;2
- 823 Puri, K. (1988). On the importance of low-frequency gravity modes for the evolution
824 of large-scale flow in a general circulation model. *J. Atmos. Sci.*, *45*(18), 2523–
825 2544. doi: [https://doi.org/10.1175/1520-0469\(1988\)045<2523:OTIOLF>2.0.CO;](https://doi.org/10.1175/1520-0469(1988)045<2523:OTIOLF>2.0.CO;2)
826 2
- 827 Rennie, M. P., Isaksen, L., Weiler, F., de Kloe, J., Kanitz, T., & Reitebuch,
828 O. (2021). The impact of Aeolus wind retrievals on ECMWF global
829 weather forecasts. *Q. J. R. Meteorol. Soc.*, *147*(740), 3555–3586. doi:
830 <https://doi.org/10.1002/qj.4142>
- 831 Sato, K., & Yamada, M. (1994). Vertical structure of atmospheric gravity waves
832 revealed by the wavelet analysis. *J. Geophys. Res. Atmos.*, *99*(D10), 20623–
833 20631. doi: <https://doi.org/10.1029/94JD01818>
- 834 Savazzi, A. C. M., Nuijens, L., Sandu, I., George, G., & Bechtold, P. (2022).
835 The representation of the trade winds in ECMWF forecasts and reanaly-
836 ses during EUREC⁴A. *Atmos. Chem. Phys.*, *22*(19), 13049–13066. doi:
837 <https://doi.org/10.5194/acp-22-13049-2022>
- 838 Skamarock, W. C., Park, S.-H., Klemp, J. B., & Snyder, C. (2014). Atmospheric kinetic
839 energy spectra from global high-resolution nonhydrostatic simulation. *J.*
840 *Atmos. Sci.*, *71*(11), 4369–4381. doi: <https://doi.org/10.1175/JAS-D-14-0114>
841 .1
- 842 Staniforth, A., Beland, M., & Côté, J. (1985). An analysis of the vertical structure
843 equation in sigma coordinates. *Atmos.-Ocean*, *23*, 323–358. doi: [https://doi](https://doi.org/10.1080/07055900.1985.9649232)
844 .org/10.1080/07055900.1985.9649232
- 845 Stoffelen, A., Pailleux, J., Källén, E., Vaughan, J. M., Isaksen, L., Flamant, P., . . .
846 Ingmann, P. (2005). The atmospheric dynamic mission for global wind mea-
847 surements. *Bull. Amer. Meteor. Soc.*, *86*(1), 73–87. doi: [https://doi.org/](https://doi.org/10.1175/BAMS-86-1-73)
848 10.1175/BAMS-86-1-73
- 849 Swarztrauber, P. N., & Kasahara, A. (1985). The vector harmonic analysis
850 of laplace tidal equations. *SIAM J. Stat. Comput.*, *6*(2), 464–491. doi:
851 <https://doi.org/10.1137/0906033>
- 852 Tanaka, H., & Žagar, N. (2020). 3d modal variability and energy transformations
853 on the sphere. In N. Žagar & J. Tribbia (Eds.), *Modal view of atmospheric*
854 *variability: Applications of normal-mode function decomposition in weather*
855 *and climate research* (pp. 121–179). Cham: Springer International Publishing.
856 doi: https://doi.org/10.1007/978-3-030-60963-4_1
- 857 Terasaki, K., Tanaka, H., & Žagar, N. (2011). Energy spectra of Rossby and gravity
858 waves. *SOLA*, *7*(1), 45–48. doi: <https://doi.org/10.2151/sola.2011-012>
- 859 Trenberth, K. E., Stepaniak, D. P., & Caron, J. M. (2000). The global monsoon as
860 seen through the divergent atmospheric circulation. *J. Climate*, *13*, 3969–3993.
861 doi: [https://doi.org/10.1175/1520-0442\(2000\)013<3969:TGMASST>2.0.CO;2](https://doi.org/10.1175/1520-0442(2000)013<3969:TGMASST>2.0.CO;2)
- 862 Tribbia, J. (2020). Normal Mode Functions and Initialization. In N. Žagar &
863 J. Tribbia (Eds.), *Modal view of atmospheric variability: Applications of*
864 *normal-mode function decomposition in weather and climate research* (pp. 63–
865 78). Cham: Springer International Publishing. doi: [https://doi.org/10.1007/](https://doi.org/10.1007/978-3-030-60963-4_1)
866 978-3-030-60963-4_1
- 867 Uccellini, L. W., & Koch, S. E. (1987). The synoptic settings and possible energy
868 sources for mesoscale wave disturbances. *Mon. Wea. Rev.*, *115*(3), 721–729.
869 doi: [https://doi.org/10.1175/1520-0493\(1987\)115<0721:TSSAPE>2.0.CO;2](https://doi.org/10.1175/1520-0493(1987)115<0721:TSSAPE>2.0.CO;2)
- 870 Žagar, N., Jelić, D., Blaauw, M., & Bechtold, P. (2017). Energy spectra and inertia-
871 gravity waves in global analyses. *J. Atmos. Sci.*, *74*, 2447–2466. doi: [https://](https://doi.org/10.1175/JAS-D-16-0341.1)
872 doi.org/10.1175/JAS-D-16-0341.1

- 873 Žagar, N., Kasahara, A., Terasaki, K., Tribbia, J., & Tanaka, H. (2015). Normal-
874 mode function representation of global 3D datasets: open-access software for
875 the atmospheric research community. *Geosci. Model Dev.*, *8*(4), 1169–1195.
876 doi: <https://doi.org/10.5194/gmd-8-1169-2015>
- 877 Žagar, N., Lunkeit, F., Sielmann, F., & Xiao, W. (2022). Three-dimensional struc-
878 ture of the equatorial kelvin wave: Vertical structure functions, equivalent
879 depths, and frequency and wavenumber spectra. *J. Clim.*, *35*(7), 2209–2230.
880 doi: <https://doi.org/10.1175/JCLI-D-21-0342.1>
- 881 Žagar, N., Neduhal, V., Vasylykevych, S., Ž. Zaplotnik, & Tanaka, H. (2023). Decom-
882 position of vertical velocity and its zonal wavenumber kinetic energy spectra
883 in the hydrostatic atmosphere. *J. Atmos. Sci.* doi: <https://doi.org/10.1175/JAS-D-23-0090.1>
- 884
- 885 Žagar, N., Tribbia, J., Anderson, J. L., & Raeder, K. (2009a). Uncertainties of
886 estimates of inertia-gravity energy in the atmosphere. Part II: large-scale equa-
887 torial waves. *Mon. Wea. Rev.*, *137*(11), 3858–3873. Corrigendum, *Mon. Wea.*
888 *Rev.*, *138*, 2476–2477. doi: <https://doi.org/10.1175/2009MWR2816.1>
- 889 Žagar, N., Tribbia, J., Anderson, J. L., & Raeder, K. (2009b). Uncertainties of
890 estimates of inertia-gravity energy in the atmosphere. Part I: intercompar-
891 ison of four analysis datasets. *Mon. Wea. Rev.*, *137*(11), 3837–3857. Cor-
892 rigendum, *Mon. Wea. Rev.*, *138*, 2476–2477. doi: <https://doi.org/10.1175/2009MWR2815.1>
- 893
- 894 Waite, M. L., & Snyder, C. (2009). The mesoscale kinetic energy spectrum of a
895 baroclinic life cycle. *J. Atmos. Sci.*, *66*(4), 883–901. doi: <https://doi.org/10.1175/2008JAS2829.1>
- 896
- 897 Wang, C. (2002). Atmospheric circulation cells associated with the El Niño-
898 Southern Oscillation. *J. Clim.*, *15*(4), 399–419. doi: [https://doi.org/10.1175/1520-0442\(2002\)015\(0399:ACCAWT\)2.0.CO;2](https://doi.org/10.1175/1520-0442(2002)015(0399:ACCAWT)2.0.CO;2)
- 899
- 900 Webster, P. (2020). *Dynamics of the tropical atmosphere and oceans*. Chichester,
901 UK: John Wiley and Sons, Ltd.
- 902 Wedi, N. P. (2014). Increasing horizontal resolution in numerical weather predic-
903 tion and climate simulations: illusion or panacea? *Phil. Trans. R. Soc. A*,
904 *372*(2018). doi: <https://doi.org/10.1098/rsta.2013.0289>
- 905 Wheeler, M., Kiladis, G. N., & Webster, P. J. (2000). Large-scale dynamical fields
906 associated with convectively coupled equatorial waves. *J. Atmos. Sci.*, *57*(5),
907 613–640. doi: [https://doi.org/10.1175/1520-0469\(2000\)057\(0613:LSDFAW\)2.0.CO;2](https://doi.org/10.1175/1520-0469(2000)057(0613:LSDFAW)2.0.CO;2)
- 908
- 909 Yang, G.-Y., Feng, X., & Hodges, K. (2023). Seasonal and interannual variation
910 of equatorial waves in ERA5 and GloSea5. *Q. J. R. Meteorol. Soc.*, *149*(752),
911 1109–1134. doi: <https://doi.org/10.1002/qj.4460>
- 912 Yang, G.-Y., Hoskins, B. J., & Slingo, J. (2003). Convectively coupled equato-
913 rial waves: A new methodology for identifying wave structures in observa-
914 tional data. *J. Atmos. Sci.*, *60*, 1637–1654. doi: [https://doi.org/10.1175/1520-0469\(2003\)060\(1637:CCEWAN\)2.0.CO;2](https://doi.org/10.1175/1520-0469(2003)060(1637:CCEWAN)2.0.CO;2)
- 915
- 916 Zurita-Gotor, P. (2019). The Role of the Divergent Circulation for Large-Scale Eddy
917 Momentum Transport in the Tropics. Part I: Observations. *J. Atmos. Sci.*,
918 *76*(4), 1125–1144. doi: <https://doi.org/10.1175/JAS-D-18-0297.1>
- 919 Zurita-Gotor, P. (2021). The interannual variability of the tropical divergence tilt
920 and its connection with the extratropical circulation. *J. Clim.*, *34*(1), 259–275.
921 doi: <https://doi.org/10.1175/JCLI-D-20-0373.1>